ANTON RUZANOV

Computational investigation
of the electrical double layer
at metal–aqueous solution and
metal–ionic liquid interfaces

TARTU ÜLIKOOL
UNIVERSITAS TARTUENSIS
1632

DISSERTATIONES CHIMICAE UNIVERSITATIS TARTUENSIS

171

ANTON RUZANOV

Computational investigation of the electrical double layer at metal–aqueous solution and metal–ionic liquid interfaces

Institute of Chemistry, Faculty of Science and Technology, University of Tartu, Estonia

The dissertation was accepted for the commencement of the degree of *Doctor philosophiae* in Chemistry at the University of Tartu on May 05th, 2018 by the Council of Institute of Chemistry, Faculty of Science and Technology, University of Tartu.

Supervisors:	Prof. Enn Lust, University of Tartu, Estonia
	Ph.D. Vladislav Ivaništšev, University of Tartu, Estonia
Consultant:	Prof. Renat Nazmutdinov,
	Kazan State University, Russia
Opponent:	Dr. Natalia Borisenko
	Institute of Electrochemistry
	Clausthal University of Technology, Germany

Commencement: June 21, 2018, at 10.15 Ravila 14A (Chemicum)

TABLE OF CONTENTS

1. LIST OF ORIGINAL PUBLICATIONS

I. **A. Ruzanov**, M. Lembinen, I.V. Voroshylova, P. Jakovits, S.N. Srirama, M. Natalia D.S Cordeiro, C.M. Pereira, J. Rossmeisl, V. Ivaništšev, On the thickness of the double layer in ionic liquids, Physical Chemistry Chemical Physics, 20 (2018) 10275–10285.

II. **A. Ruzanov**, M. Lembinen, H. Ers, J.M. Garsía de la Vega, I. Lage-Estebanez, E. Lust, V. Ivaništšev, DFT Study of Ionic Liquids Adsorption on Circumcoronene Shaped Graphene, Journal of Physical Chemistry, 122 (2018) 2624–2631.

III. **A. Ruzanov**, K. Karu, V. Ivaništšev, R. R. Nazmutdinov, E. Lust, Interplay between the hydrophilicity of metal electrodes and their interfacial capacitance, Electrochimica Acta, 210 (2016) 615–621.

IV. I. Lage-Estebanez, **A. Ruzanov**, J.M. Garsía de la Veja, M.V. Fedorov, V. Ivaništšev, Self-interaction error in DFT-based modelling of ionic liquids, Physical Chemistry Chemical Physics, 18 (2016) 2175–2182.

Author's contribution:

Paper I: Performed all calculations and interpretation of results. Responsible for writing of the manuscript.

Paper II: Performed DFT calculations, analyses and modelling. Responsible for planning and writing of the manuscript.

Paper III: Performed DFT calculations, analyses and modelling. Responsible for planning and writing of the manuscript.

Paper IV: Performed DFT calculations and modelling. Responsible for the graphics and writing.

2. LIST OF ACRONYMS AND NOTATIONS

ab initio – a Latin term meaning "from the first principles"

et al. – a Latin term meaning "and others"

in situ – a Latin term meaning "localised at the interface"

DFT – density functional theory

EDL – electrical double-layer

EA – electron affinity

MD – molecular dynamic (simulation)

MFA – mean field approximation

pzc – potential of zero-charge

RTIL – room-temperature ionic liquid

SIE – self-interaction error

HOMO – highest occupied molecular orbital

ChelpG – Charges from Electrostatic Potentials using Grid-based method

B3LYP – Becke three-parameter Lee–Yang–Parr functional

D3 – Grimme's dispersion correction

gCP – geometrical counterpoise correction

PBE – Perdew–Burke–Ernzerhof functional

PBEh-3c – reparametrised version of PBE functional

E_{ads} – adsorption energy

E_{int} – interaction energy

E_{diss} – dissociation energy

μ – dipole moment

F – electric field

ρ – total charge density

C – capacitance

U – potential

σ – surface charge density

$EMIm^+$ – 1-ethyl-3-methylimidazolium cation

BF_4^- – tetrafluoroborate anion

PF_6^- – hexafluorophosphate anion

$AlCl_4^-$ – tetrachloroaluminate anion

3. INTRODUCTION

Interfaces between solid surfaces and aqueous solutions are among the most frequently encountered in nature and technology. Accordingly, they are in the focus of intensive studies in the fields of heterogeneous catalysis, electrochemistry, and geochemistry [1]. The so-called room temperature ionic liquids (RTILs) have properties that are superior to those of aqueous solutions, and for this reason, they also attract an increasing research interest [2–4]. A detailed understanding of the structure, thermodynamics and kinetics of RTILs at electrode surfaces becomes essential for designing modern electrochemical devices [5–11].

In this work, we choose computational methods to model both metal–aqueous solution and metal–ionic liquid interfaces [1]. The former was modelled extensively in the past, while at the beginning of this work, there were only a few quantum chemical studies of the latter [12,13]. Thereby, we aimed to take the lead in the computational studies of the metal–ionic liquid interfaces. Our primary goal was to provide complementary data to the experimental studies held at the University of Tartu [14–17]. We started with the simplest models of the interfaces and gradually increased their complexity. In the beginning, the central hypothesis relied on the additivity principle. We divided the interface into distinct structural regions to evaluate the corresponding properties assuming that their sum gives an experimentally measured quantity, such as the differential capacitance. The challenge was in the estimation of the potential drop across the interface. In progress, we coined the idea of the interfacial dipole – an efficiently computed quantity that substitutes the potential drop. The interfacial dipole concept is uncommon to the field of electrochemistry. One of the rare electrochemical quantum studies, Ref. [18], was mainly cited in the field of organic heterojunctions. In the thesis, we apply the concept solely in the electrochemical context. In the following chapters, we illustrate how the interfacial dipole can be split into the components as well as used to evaluate both the potential drop and the capacitance of the metal–electrolyte interface.

Chapter 4 of the thesis presents a quantum chemical study of the interfacial structure and differential capacitance of the electrical double layer

(EDL) in aqueous solution at Bi(111), Ga, and Hg surfaces. The latter is of great interest for testing novel conceptions and theories of the EDL [19]. In this study, we aimed to highlight the vital contribution of the adsorbed water molecules to the interfacial dipole and the differential capacitance. Chapters 5–7 of the thesis present quantum chemical studies of the electrode–RTIL interfaces. Chapter 5 provides computational insights into the structure of the Au(111)–EMImBF$_4$ interface and how it influences the interfacial dipole as well as the differential capacitance. Chapter 6 presents the data for the interfacial dipole formed between six ionic pairs and a C$_{54}$H$_{18}$ surface. Chapter 7 finalises the work by comparing the behaviour of EMImBF$_4$ ionic associates at Au(111), Bi(111), and C$_{54}$H$_{18}$ surfaces, focusing again on the components of interfacial dipole and the differential capacitance values.

3.1 Main aim of studies

Overall, this work aims to show that one of the main properties of the EDL – the potential drop at the metal–electrolyte interface – can be alternatively represented as an interfacial dipole. It is more convenient for analysing the computational results. The interfacial dipole can be coherently divided into components that represent specific structural layers of the EDL. By analysing these components, we demonstrate that the conceptual difference between the aqueous and RTIL interfacial properties is dictated by the difference in their molecular/ionic structure. Similarly, the interfacial dipole concept can be utilised in computational studies to explain a wide variety of interfacial phenomena.

4. ELECTRICAL DOUBLE LAYER AT METAL–AQUEOUS SOLUTION INTERFACE

Being the most common solvent in nature, water is involved in various technological processes related to different fields of electrochemistry. Solid–water interfaces have been intensively studied using various methods, including computer simulation techniques [1]. The majority of computational approaches has been employed to describe the H_2O behaviour at Pt, Pd and Cu surfaces [20]. Much attention has been devoted to *d*- and *sd*-metals due to a persistent need for cheaper catalysts in faradic electrochemistry [21]. At the same time, less attention has been paid to the analysis of catalytically inactive *sd*- and *p*-metals. These metals are of great interest for non-faradic electrochemistry and are commonly studied to examine novel conceptions and theories of the EDL [19].

In particular, the dependence of differential capacitance on the electrode potential is known to be influenced by the metal–water interaction [22]. At negatively charged electrodes the dependence is almost the same for many catalytically inactive metals in non-specifically adsorbing aqueous electrolytes. These two experimental facts have triggered a series of studies on gallium, mercury, and single-crystal bismuth electrodes [22,23]. Recently we have performed quantum chemical calculations combined with a three-state dipole lattice model to calculate the differential capacitance values for the EDL compact layer at Bi(111), Ga and Hg surfaces [24,25]. We accounted for various types of chemical bonding at the interface and the possibility of reorientation of water dipoles with changing the surface charge density. Our approach proved to be useful to untangle the problem of hydrophilicity of these metals [25]. The results reproduce the experimental dependence of the EDL capacitance on the surface charge density.

4.1 Computational methods

DFT calculations were performed using the Becke three-parameter Lee–Yang–Parr functional (B3LYP) as implemented in the Gaussian 09 program [26]. The Hay–Wadt effective core potential was used for all metal atoms. Valence electrons of Bi, Ga and Hg atoms were described by LanL2DZ basis

set [27]. For Bi atoms, the basis set was also augmented by polarization functions [28]. The standard basis set 6-31G(*d*,*p*) was used for O and H atoms. Gallium and mercury surfaces were presented by cluster models, where the nearest atom–atom distance was chosen to be 0.29 nm for Ga [29], and 0.30 nm for Hg [30]. Bismuth surface was modelled by clusters for which the distance and the angle between the neighbouring metal atoms are equal to the Bi bulk values (0.307 nm, 95.54°) [31].

The metal–H_2O binding energy (ΔE_{ad}) was calculated as follows:

$$\Delta E_{ad} = E_{cluster-H_2O} - E_{cluster} - E_{H_2O} \tag{1}$$

where E denotes the total energy of a chemical structure, which depends on the geometry, orientation, and on the applied electric field (F) [26].

The electric field was treated through finite-field DFT method implemented in the Gaussian program suite [26,32]. The adsorption energy *vs.* the surface charge density dependencies were calculated using the dipole lattice model. The model takes into account the effect of the electric field on three orientations of the H_2O molecule: parallel to the surface (H-par, $\theta = 90°$); H-atoms pointed toward the surface (H-down, $\theta = 180°$), and O-atom pointed toward the surface (H-up, $\theta = 0°$, Figure 1). The orientation of H_2O was described by z_0 and θ values (Figure 2), where z_0 is the optimized surface plane–O distance and θ is the tilt angle of the H_2O molecule relative to the surface normal.
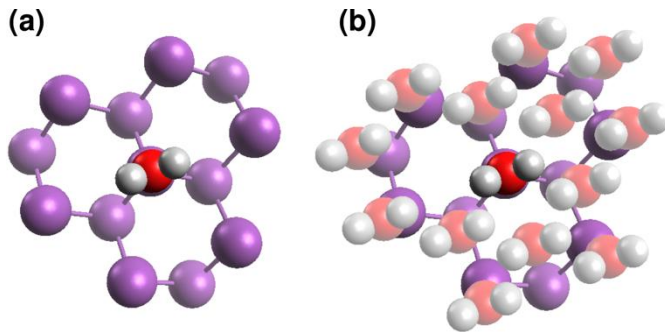

Figure 1. (a) A single H_2O molecule, adsorbed at the bismuth cluster in H-up orientation (top view). (b) Dipole lattice model in which each H_2O molecule is represented as a dipole, while only the central H_2O molecule–metal interaction is taken into account.
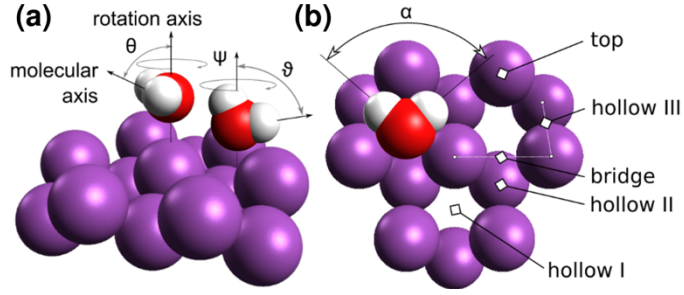
Figure 2. (a) Side and (b) top views of different adsorption sites at the model metal clusters used to describe the adsorption of H_2O molecule at a Bi(111) surface cluster. The bond angle α characterizes the internal geometry of the molecule, and the rotation angles θ, ψ and ϑ characterize orientation of the molecule relative to the surface normal labeled as "rotation axis".

The reorientation energy ($\Delta\Delta E_{ad}$) was defined as:

$$\Delta\Delta E_{ad}(\text{H-up/down}) = E_{ad}(\text{H-down}) - \Delta E_{ad}(\text{H-up}) \qquad (2)$$

The dipole lattice model, describing the behaviour of the water molecules at a polarizable interface was developed by Schmickler [33]. In this model, a single H_2O molecule interacts with an effective field (F) of the H_2O mono-layer. As explained below, the lattice dipole model describes the contribution of the adsorbed water molecules to the interfacial dipole characteristics. More detailed analysis of the approach used here can be found elsewhere. [33–35].

4.2 Results and discussion

4.2.1 Compact layer capacitance

External chemical potentials determine the interfacial structure. Thus, such EDL properties as the surface charge density (σ), potential drop ($\Delta\varphi$), and the internal electric field (F) satisfy the thermodynamic constraints imposed by the environment. These closely interrelated properties can be represented regarding an interfacial dipole (μ):

$$\Delta\varphi = \frac{\mu}{\varepsilon_0 A} \tag{3}$$

$$\sigma = \frac{\mu}{dA} \tag{4}$$

$$F = \frac{\mu}{\varepsilon_0 dA} \tag{5}$$

where ε_0 is permittivity of vacuum, A is a surface area that holds a quantity of charge (q), μ is dipole moment, and d is the distance between the surface charge planes at the electrode and in the electrolyte.

It is not trivial in computations to set adequate thermodynamic constraints. More commonly, constant surface charge, constant potential difference or constant applied field are used to cause the EDL formation. In this study, we chose the applied electric field.

The differential capacitance of the EDL compact layer (C_H) can be expressed in the following way:

$$\frac{1}{C_H} = \frac{\partial\Delta\varphi_H}{\partial\sigma} = \frac{\partial\Delta\varphi_v}{\partial\sigma} - \frac{\partial\Delta\varphi_w}{\partial\sigma} - \frac{\partial\Delta\varphi_{Me}}{\partial\sigma} = \frac{1}{C_v} - \frac{1}{C_w} - \frac{1}{C_{Me}} \tag{6}$$

where the potential drop in the compact layer ($\Delta\varphi_H$) to the first approximation is divided into three components – three potential drops: between the surface charge plane and the ionic charge plane ($\Delta\varphi_v$), due to the water monolayer formation ($\Delta\varphi_w$), and due to a shift in the electronic density at the metal surface layer ($\Delta\varphi_{Me}$).

Several sets of data were used to calculate the capacitances including water adsorption energy (Eq. 1) and the metal cluster highest occupied molecular orbital (HOMO) values at different applied electric fields (F).

The metal capacitance (C_{Me}) is defined as follows:

$$C_{Me} = \frac{F\,\partial\sigma}{\partial\Delta\varphi_{Me}} \approx \frac{F\,\partial\sigma}{\partial\sum_i p_i\varepsilon_i} \tag{7}$$

where F is the Faraday constant, ε_i is the HOMO energy values of a metal cluster model with a specifically oriented water molecule (H-up, H-par,

H-down) and p_i is the statistical weight of adsorbed water molecules in a given orientation.

The water layer capacitance (C_w) is expressed as:

$$C_W = \frac{F \, \partial\sigma}{\partial\Delta\varphi_W} = \frac{\varepsilon_0}{\rho_W \mu} \frac{F \, \partial\sigma}{\partial(p^{\text{H-up}} - p^{\text{H-down}})} \qquad (8)$$

where $(p^{\text{H-up}} - p^{\text{H-down}})$ is the difference between the statistical weights of the H-up and H-down orientations for H_2O molecules, ε_0 is the permittivity of vacuum, ρ_w is the surface density of the H_2O molecules, and μ is the dipole moment of H_2O molecule.

The vacuum capacitance (C_v) is given as:

$$C_V = \frac{F \, \partial\sigma}{\partial\Delta\varphi_V} = \frac{F \, \partial\sigma}{\varepsilon_0 \, \partial(\sum_i p_i z_i(\text{Me} - \text{O}) + z_{\text{ion}} - z_{\text{Me}})\sigma} \qquad (9)$$

where $z_i(\text{Me–O})$ is the optimized surface plane–O distance for a given orientation of the H_2O molecule, z_{ion} is the distance from $z_i(\text{Me–O})$ to the plane, where the centres of the hydrated ions are located, z_{Me} is the distance between the surface plane and the surface charge plane.

The dependence of the surface charge plane position on the electrode surface charge density was described by Eq. 7, which takes into consideration also the influence of the H_2O molecule adsorption on the metal electron density distribution. Accounting for the surface charge plane position (z_{Me}), in addition to the calculated $\Sigma p_i z_i(\text{Me–O}) + z_{\text{ion}}$ distance, results in considerably higher capacitance values.

The contact adsorption phenomenon is frequently used to explain the anomalously high interfacial capacitance values. However, for example, Fawcett and Ryan showed that the contact adsorption of perchlorate anions does not need to be involved in the explanation of the high C_H values observed at a mercury electrode [36], despite the common belief that the perchlorate anion is surface active and adsorbs specifically. Similarly, explanation of the high C_H values observed at a gallium electrode does not

require speculations with specific adsorption of neither ions nor water molecules and can be explained by electrostatics with a correction of z_{Me} and rigorously defined distance of the closest approach, *e.g.* as $\Sigma_i p_i z_i(\text{Me–O}) + z_{\text{ion}}$.

For surface inactive ions, the distance of the closest approach can be obtained based on molecular dynamic simulations and are within the range of 0.4÷0.5 nm [37,38]. The ion density distribution profile in the vicinity of a metal electrode shows that most of Na^+ ions are located around the plane at 0.43 nm distance and most of F^- – around 0.47 nm from the surface. Thus, no contact adsorption of Na^+ and F^- occurs in the simulations at moderate negative and positive surface charge densities. The molecular dynamics simulations predict that non-specifically adsorbing ions situate over the first interfacial layer of H_2O molecules. In our model, the position of counter-ion above the O-plane (z_{ion}) is considered as a common feature and is switched between anion and cation values by a sigmoid fitting function.

The compact layer differential capacitance curves obtained experimentally are shown in Figure 3b. Going from negative to positive surface charge densities the C_H values increase more rapidly for gallium than those of Bi and Hg [19]. The humps in the $C_H(\sigma)$ dependence lie far above experimentally measurable surface charge densities, except for the one measured on mercury electrode (Figure 3b). The humps are visible in the calculated $C_H(\sigma)$ dependence shown in Figure 3a. Within the range from -15 to $+15$ µC/cm^2, the C_V determines the magnitude of the calculated compact layer capacitance, whether the C_w contributes to the capacitance response to surface charging, *i.e.* is responsible for the appearance of the humps. Analysis of statistical weights (Figure 4) of three different orientations (H-down, H-par and H-up) shows the connection between the hump position on the capacitance plot and the water dipole reorientation in an external field.

As can be seen from Figure 4, the contribution of the parallel orientation (H-par) of water molecules decreases in the row Ga > Bi(111) > Hg. For Ga–solution interface the dipole orientation distribution is more symmetric around the H-par than for Bi(111)–solution and Hg–solution interfaces; and at very low and very high surface charge density values the H-down and H-up orientations prevail, respectively.

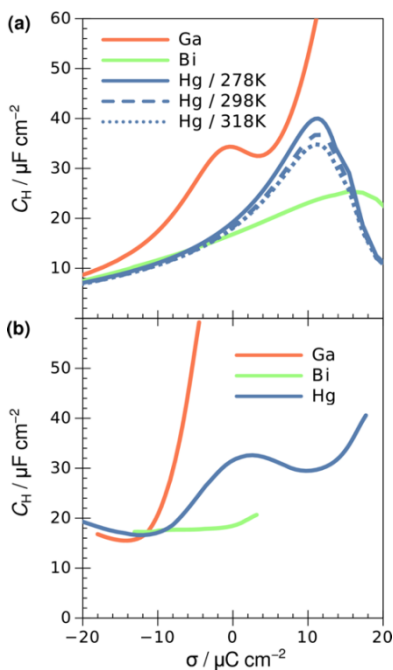**Figure 3.** (a) Calculated and (b) measured $C_H(\sigma)$ dependencies for Bi(111), Ga and Hg electrodes. The corresponding experimental data are taken from Refs. [39–41].
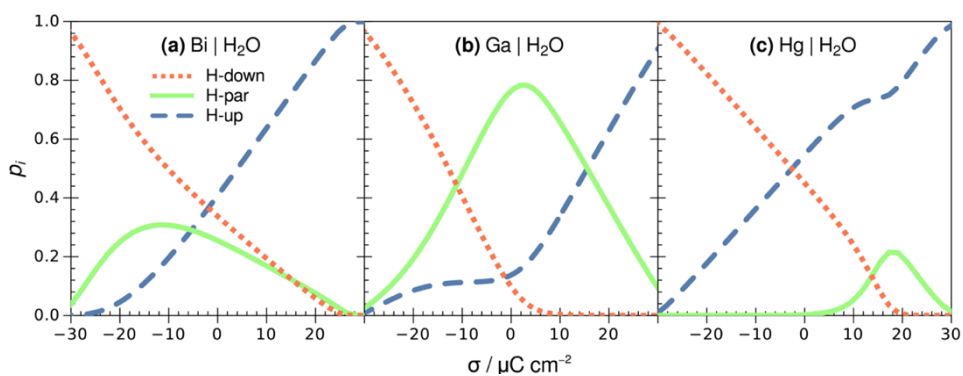

Figure 4. Statistical weights (p_i) of adsorbed water molecules in a given orientation (H-up, H-down, H-par) depending on the electrode surface charge density, calculated for (a) Bi(111), (b) Ga and (c) Hg electrodes.

The latter is directly reflected in the dependence of the mean orientation along the field direction as a function of the surface charge density and leads to so-called saturation that is responsible for the capacitance decrease upon lowering or increasing the surface charge density to very high absolute values. Here, according to Eqs. 6 and 8, the derivative of the surface charge density over the potential drop in the water monolayer becomes larger when the $p^{\text{H-up}} - p^{\text{H-down}}$ change is small. The difference between the statistical weights of the H-up and H-down orientations for H_2O molecules is indeed smaller for gallium because most of the H_2O molecules are reoriented for the parallel orientation to either H-up and H-down orientations. At Bi(111)–solution and Hg–solution interfaces the reorientation mostly takes place from H-up directly to H-down orientation and *vice versa*. Therefore, the hump on the $C_H(\sigma)$ dependence for Ga–solution interfaces observed at negative σ values is related to the preferred in-plane orientation of the H_2O molecules as well as low reorientation barrier for H_2O molecules at Ga.

It is useful to mention other explanations reported in the literature. Foremost, the significantly higher EDL capacitance for gallium–aqueous electrolyte interface was explained by the chemisorption of H_2O molecules [36,42].

The chemisorption implies the appearance of adsorbed water molecules oriented with their negative end towards the electrode surface (H-up orientation) that leads to an increase in the C_H capacitance values at positive electrode charges due to peculiar dipole contribution and also due to smaller metal–water distances of the closest approach [43]. Firstly, it should be noted that the H-up orientation has a non-zero probability for Bi(111), Ga and Hg electrodes within the whole range of surface charge values studied, not only in the vicinity of the C_H maxima. Secondly, the metal–water distance of the closest approach increases in the order: Bi(111)–H_2O (0.23 nm) < Ga–H_2O (0.26 nm) < Hg–H_2O (0.30 nm) (summarised in Table 1). Finally, the adsorption energy value of H_2O at Ga is smaller than at Bi(111) and Hg, which does not confirm the hypothesis of the H_2O chemisorption at the Ga surface.

Table 1. Averaged adsorption energies (ΔE_{ad} / kJ mol^{-1}) for the H_2O molecule adsorption in H-up orientation at optimized z_0 distances. Estimated reorientation energies ($\Delta\Delta E_{ad}$ / kJ mol^{-1}) for the different adsorption sites. Presented mean values have been averaged over the results obtained for different clusters.

clusters	Site	z_0, nm	$-\Delta E_{ad}$(H-up)	$\Delta\Delta E_{ad}$
Bi	hollow	0.23	27	14
Ga	top	0.26	23	10
Hg	top	0.30	34	17

Overall, we suggest that the reasons for the hump on the $C_H(\sigma)$ plots could be attributed to the nonlinear response of molecular reorientations and the electronic profile at the metal surface. Note that according to our calculations both of these effects were found to take place. The chemisorption of water molecules at Bi(111), Ga and Hg electrodes most probably do not contribute to the interfacial capacitance. We have found that the H_2O adsorption at all metal surfaces considered does not reveal the chemisorption features such as covalent bonding and high absolute H_2O–surface atoms interaction energy value. In contrast, the analysis of the electron density difference exhibits a simple donor–acceptor mechanism, and the calculated H_2O–metal interaction strength (Table 1) is comparable to the strength of H-bonding.

4.3 Conclusive remarks

We have combined DFT calculations with the mean field theory to evaluate the compact layer capacitance at the Bi(111), Ga and Hg electrodes. The obtained compact layer capacitance (C_H) *vs.* surface charge density (σ) curves agree with the experimental differential capacitance measurements data. In particular, according to our results, the rise in the C_H *vs.* σ dependence with increasing the surface charge density is remarkably steeper for Ga than those calculated for Bi and Hg. This result does not corroborate the earlier hypothesis about the strong chemisorption of water molecules at the gallium electrode surface [42]. The layer formed by the adsorbed water has a dipole that strongly depends on the surface charge density and largely contributes to the total interfacial dipole. Thus, we can conclude that the observed difference in the C_H *vs.* σ dependence for Bi(111), Hg and Ga is due

to the ability of adsorbed water molecules to reorient in response to the electrode charging with a variation of potential with respect of zero charge potential.

The obtained results highlight the significant role of the interfacial water layer characteristics in the interfacial properties of metal surface–electrolyte solution interface. The model incorporates three types of dipoles that sum into the interfacial dipole: the surface dipole of the electrode, the ionic dipole between the region of the surface charge plane and the ionic charge plane, and the water layer dipole. The latter parameter depends on the surface charge more strongly than the other two. Therefore, the water reorientation within this thin layer determines the shape of the capacitance curve depending on the surface charge density, electrode potential or applied field.

5. ELECTRICAL DOUBLE LAYER AT GOLD–IONIC LIQUID INTERFACE

Since their rediscovery in the 1990s, the so-called RTILs attract considerable research interest in the fields of surface science and physical chemistry, due to combinations of physicochemical properties that make them excellent candidates for a wide range of applications [2–4]. A particular combination of properties results from a subtle balance of Coulomb and van der Waals interactions, donor-acceptor bonds, conformational flexibility, and steric effects. Therefore, a task-specific set of properties can be achieved by structural variations and selection of the right combination of ions. Recently, the interfacial properties of RTILs have attracted considerable attention. Currently, the EDL at the electrode–RTIL interfaces is in focus of research on enhancing the performance of energy storage and transformation in supercapacitors [5,6], actuators [7,8], batteries [9,3], solar cells [10], and fuel cells [11].

Molecular physics and computational chemistry are playing a significant role in the exploration of the IL properties-landscape depending on the chemical composition. In particular, because of the continuous increase in computing power, the use of quantum chemical methods becomes more and more attractive for studying the electronic structure and reactivity of ILs. Due to the favourable accuracy-to-computational cost ratio, DFT methods are most actively used for the calculations of electronic structure of ILs and MD force fields for parametrization of ILs.

5.1 Literature overview

Significant progress in the understanding of the interfacial processes occurring in the EDL has been made recently at the theoretical level [44–49], by computational modelling [50–56], and in experimental measurements [17,57–71]. Nevertheless, some authors argue whether the EDL at electrode surface in RTILs is *one* or *multi* ionic-layer thick. On the one hand, by vibrational Stark shifts and capacitance measurements, Baldelli concluded that the EDL in RTILs is effectively one ion-layer thick due to a

single layer of counter-ions [61,62]. On the other hand, other authors considered a multilayer structure for interpretation of electrochemical impedance data [63,65]. MD simulations [72–74,55], atomic force microscopy [75], and X-ray spectroscopy [76–78] studies have ascertained that the EDL in RTILs indeed consists of alternating layers of anions and cations. According to these studies, in the innermost layer, the counter-ions are in direct contact with the surface, templating the subsequent layers. Upon closer examination of MD simulations results, it appears that the EDL structure changes from *multi-* to *mono*layer upon variation of the surface charge density [54,56]. Does the innermost layer dominate in the overall potential-dependent multilayer EDL?

To answer this question, we focused on the adsorption of BF_4^- anions from 1-ethyl-3-methylimidazolium tetrafluoroborate (EMImBF$_4$) ionic liquid on Au(111) surface. First, we examined the differences in DFT and MD representation of the Helmholtz model of the Au(111)–BF_4^- interface. Then, we compared the Helmholtz model with a more realistic structure using MD simulations accounting the layering of ions at the Au(111)–EMImBF$_4$ interface.

The interfaces between imidazolium tetrafluoroborate and single crystal Au(111), Cd(0001), Bi(111) as well as polycrystalline gold and platinum surfaces were previously studied using cyclic voltammetry and impedance spectroscopy techniques [65,17,66–68,71,79–83]. The capacitance dependence on potential established is determined by the adsorption of anions/cations, implying accumulation of ionic counter charge near the charged metal surface. For some ions, the formation of the ordered adlayers at single-crystal gold faces was observed by *in situ* scanning tunnelling microscopy [71,84–87]. Thus, we assumed that an ordered layer of BF_4^- describes the Au(111)–EMImBF$_4$ interface mainly at positive surface charge densities.

5.2 Computational methods

5.2.1 Interface models

As a rough approximation of a positively charged electrode immersed into an EMImBF$_4$ ionic liquid, we constructed a set of Au(111)–BF$_4^-$ interface configurations representing the Helmholtz EDL model. In this model, the surface charge is compensated by a layer of counter-ions at an average distance d from the metal surface. This model represents a simple parallel plate capacitor, where metal is taken as an ideal conductor.

BF$_4^-$

EMImBF$_4$ pair

EMImBF$_4$ crystal

Au(111) | EMImBF$_4$ interface
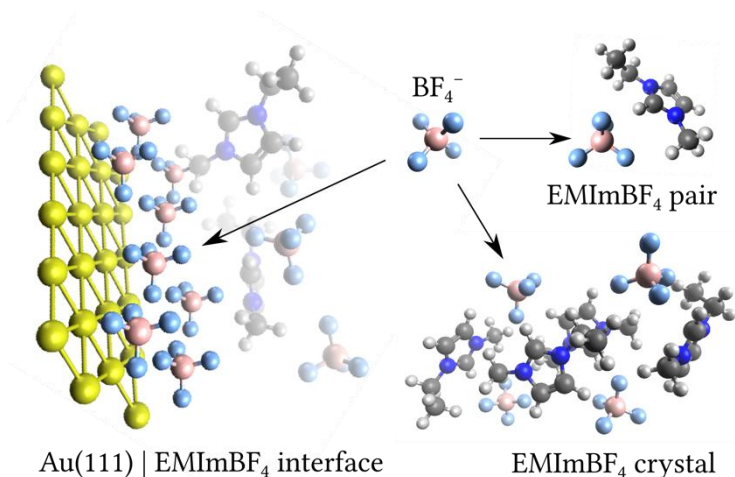
Figure 5. BF$_4^-$ structure at the Au(111) | EMImBF$_4$ interface; in EMImBF$_4$ crystal and forming a pair with EMIm$^+$ cation. The interface model shows √3×√3 BF$_4^-$ adlayer adsorbed on Au(111) (monolayer model) with an additional EMImBF$_4$ layer drawn as semi-transparent (multilayer model).

In the DFT calculations, the coverage (θ) ranged from 1/20 to 1/2 of BF$_4^-$ anions per surface gold atom in the unit cell of variable size. Three layers of gold atoms in total formed the slab representing the Au(111) surface. Figure 6a shows the Au(111)–BF$_4^-$ interface model at $\theta = 1/3$. Only the first upper Au layer was allowed to relax, while the two bottom layers were kept fixed in their bulk positions. As a starting guess point for the electronic structure simulations, a varying number of BF$_4^{\cdot}$ radicals were placed on the neutral Au(111) surface. During relaxation the charge on the radicals spontaneously decreased, finally turning the BF$_4^{\cdot}$ radicals into BF$_4^-$ ions. Consequently, the

interface became polarised, and the electric field set up between the charged gold surface and adsorbed ions.

Figure 6. a) Au(111) | BF_4^- interface model at surface coverage $\theta = 1/3$. b) BF_4^- spontaneously dissociates and reorients at the same surface coverage. Only the upper, *i.e.* relaxed layer of gold is shown.

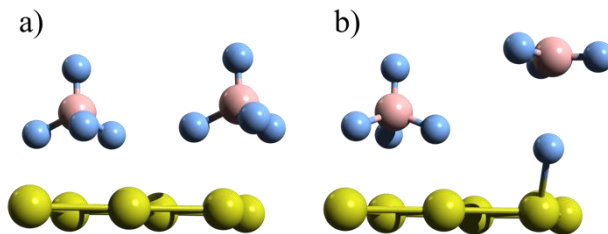Within the Helmholtz model framework, we look only at the adsorption of anions on the Au(111) surface, in the absence of cations. This divide-and-conquer approach is a reasonable first step towards more complex models. According to Ref. [88], the current model is the simplest "1D" representation of the EDL in RTILs. Recent MD simulations results reveal that the EDL structure can indeed be reduced to "1D" at a certain surface charge when a monolayer of counter-ions at a charged surface is formed [56,89]. Thus, the Helmholtz model was utilized not only to test its limits but also to verify the concept of the monolayer formation.

In the MD simulations of the Helmholtz model, a variable number of BF_4^- anions (from 1 to 112) were put into contact with a fixed Au(111) slab. The cell size was 4.04×4.00 nm^2 and consisted of 224 gold atoms. Each anion had a total charge of $-e/\sqrt{2}$, and each gold atom had a fixed point charge required to compensate the overall ionic charge. The surface charge density was varied from 1 to 80 μC/m^2 corresponding to the coverage of 1/2.

In the more realistic MD simulations, the initial configurations were constructed using the PACKMOL package [90], by inserting 288 cations and 288 anions of EMImBF$_4$ at random positions between two golden slabs to form the final simulation cell, with dimensions of 2.98 nm $\times$ 2.95 nm $\times$ 11.36 nm. The completed slab of Au(111) was setup using 480 gold atoms with the help of atomic simulation environment [91] and was fixed in positions during all simulations. The polarisation was realised by applying

an electric field in the *z*-direction of the simulation cell. According to our preliminary tests, this approach is equivalent to the assigning of point charges (as in the case of the Helmholtz model), but it is computationally more efficient. Computational details and the MD simulation parameters used in this study can be found in Ref. [92].

5.2.2 Density functional theory calculations

All DFT calculations were performed with the atomic simulation environment interface using the revised Perdew–Burke–Ernzerhof (RPBE) exchange–correlation functional that accounts for van der Waals (vdW) interactions, and projector augmented wave (PAW) method as implemented in the real-space grid code GPAW [91,93,94]. Wave functions, potentials, and electron densities were represented on grids with a spacing of approximately 0.16 Å. Brillouin-zone integrations were performed using an $a \times b \times 1$ Monkhorst-Pack *k*-point sampling grid, where *a* and *b* equal 2 or 4 depending on the size of the surface lattice cell assumed. Molecules were computed in a large non-periodic cell while the surface lattice cell was repeated periodically in the surface plane to create an infinite metal slab. Dipole correction was employed in the perpendicular direction to the slab to decouple two adjacent images electrostatically. The structural optimisations were performed with a convergence criterion of 0.05 eV/Å for atomic forces.

The starting geometry for $EMIm^+$–BF_4^- ionic pair and lattice parameters for $EMImBF_4$ crystal were taken from supporting information in Refs. [95–97] and optimised with RPBE+vdW.

The dissociation energy for $EMIm^+$–BF_4^- ionic pair -344 kJ/mol agrees with the post-Hartree–Fock results [95,98]. The energy of $EMImBF_4$ crystal dissociation into single ions is 161 kJ/mol lower. It is in agreement with the experimentally determined value for $EMImBF_4$ liquid evaporation energy (135–149 kJ/mol at 298 K) [99,100].

The binding energy values of BF_4^- in the modelled systems are expressed relative to the potential energy of BF_4^- in a vacuum, and corrected by the $BF_4^{\cdot}$ radical adiabatic electron affinity (EA) [101]:

$$\langle \mathrm{BF}_4^- \rangle = \frac{E(N,n) - E(N,0) - nE(\mathrm{BF}_4^-) - n\mathrm{EA}(\mathrm{BF}_4^{\bullet})}{n} \qquad (10)$$

where n and N are the numbers of ions and surface metal atoms in the simulated cell, respectively, and $E(N,0)$ and $E(N,n)$ are the potential energies of the bare Au(111) surface, and the charged Au(111) surface with n BF_4^- anions in the cell. The RPBE+vdW adiabatic electron affinity of $\mathrm{BF}_4^{\bullet}$ (634 kJ/mol) agrees well with the CCSD(T) value (649 kJ/mol) [102].

The $E(\mathrm{BF}_4^-)$ term can be directly related to the Madelung energy of BF_4^- in the EMImBF_4 crystal (E_{cr}) which may be considered as an approximation to the electrochemical potential of the anion in the RTIL. The formation energy of a vacancy in the EMImBF_4 crystal is expressed as follows [103]:

$$E_{\mathrm{cr}}(\mathrm{BF}_4^-) = E(\mathrm{EMImBF}_4) - E(\mathrm{BF}_4^-) - E(\mathrm{EMIm}^+) \qquad (11)$$

where $E(\mathrm{EMImBF}_4)$ is the potential energy of the EMImBF_4 crystal, and $E(\mathrm{EMIm}^+)$ is the potential energy of EMIm^+ in a vacuum. Once an anion leaves the crystal, it can be deionised to $\mathrm{BF}_4^{\bullet}$ and then it can adsorb on the Au(111) surface.

For the Au(111)–BF_4^- interface, the integral free energy change per surface metal atom (ΔG_{int}) was defined as [104–106]

$$\Delta G_{\mathrm{int}} \approx \frac{nE_{\mathrm{surf}}(\mathrm{BF}_4^-) - nE_{\mathrm{cr}}(\mathrm{BF}_4^-)}{N} \qquad (12)$$

The *integral* capacitance (C) was determined in four methods from the integral free energy, work function, ionic charges, and interfacial dipole moment. Firstly, using the classical relation:

$$C_{\mathrm{G}} = \frac{2\Delta G_{\mathrm{int}}}{\Delta U^2} \qquad (13)$$

where ΔG_{int} is equal to the energy stored in an ideal capacitor electrode which, in our case, is set up by BF_4^- ions and the counter charge on the metal surface. Here, $\Delta U = U - U_{\mathrm{pzc}}$ is the relative electrode potential calculated from the work function ($U = W_{\mathrm{e}}/e$), and U_{pzc} is the potential of zero charge (pzc). The U_{pzc} was set to be equal to the calculated work function of

the Au(111) surface (5.08 V), which is slightly lower than the experimental value of 5.26 V [107].

Secondly, taking into account that each anion brings a charge of q to the surface, capacitance C_θ can be calculated as:

$$C_\theta = \frac{qe\theta}{A\Delta U} \tag{14}$$

where A is the area of the cell, θ is surface coverage, e is elementary electronic charge, and the ionic charge (q) was obtained by the density derived electrostatic and chemical (DDEC) method [108,109].

Thirdly, taking into account the interfacial dipole moment (μ), the dipole layer capacitance C_μ can be calculated as:

$$C_\mu = \frac{qe\varepsilon_0}{\mu} \tag{15}$$

where ε_0 is the permittivity of vacuum.

Finally, assuming that the system is a parallel plate capacitor,

$$C_H = \frac{\varepsilon\varepsilon_0}{d} \tag{16}$$

where ε is the high-frequency dielectric constant of 2.0 (is typical for RTILs [110] and used to account for the electronic polarisation), and d is the distance from the position of the nearest layer of Au nuclei to the layer of B nuclei. Eq. 16 is derived based on the Helmholtz model assumptions.

5.3 Computational results

5.3.1 Au(111)–BF_4^- interface model

To obtain a qualitative comparison of the preferred orientation of a single BF_4^- ion, the usual adsorption sites on the surface were considered: face-centered cubic (fcc) and hexagonal close-packed (hcp) hollow, bridge and top sites (Figure 7). At 1/20 coverage, the fcc and hcp hollow sites were found to be the most stable adsorption sites with a negligible energy difference. At the same time, the translational movement of BF_4^- from an fcc to

an hcp hollow site requires overcoming an energy barrier of 11 kJ/mol. It was calculated that up to coverage of 1/3, the orientation of anion with three fluorine atoms pointing towards the Au(111) surface is the most favourable. At higher coverages during the geometry optimisation, the reorientation of anions can take place.
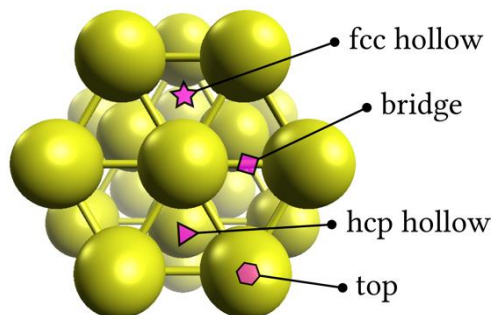

Figure 7. Investigated $BF_4^{\cdot}$ adsorption sites at Au(111) surface.

Figure 8 demonstrates the dependence of the integral free energy (G_{int}) of BF_4^{-} anions on the relative electrode potential squared (ΔU^2). A linear dependence is seen, which means that the modelled Au(111)–BF_4^{-} interface behaves as a parallel plate electrode (capacitor). The results also indicate a strong potential dependence on the orientation of BF_4^{-} ions. As it follows from the calculations, the formation of the $\sqrt{3}\times\sqrt{3}$ ordered adlayer (Figure 6a, $\theta = 1/3$) occurs at 4.6 V relative to the pzc (Figure 8, Table 2). However, the formation of the $\sqrt{3}\times\sqrt{3}$ adlayer with half of the anions flipped and dissociated (Figure 6b) can take place at a considerably lower potential of 3.5 V (Figure 9).

Table 2. Relative electrode potential (ΔU) values calculated for different surface coverages using MD simulations assuming the Helmholtz (MD_H) and multilayer (MD_{ML}) models. The DFT based values are given for comparison.

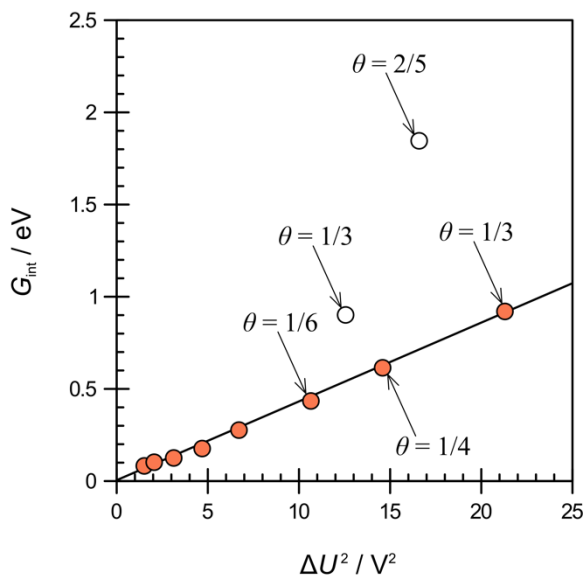| θ	DFT	MD_H	MD_{ML}
1/3	4.6 V	5.3 V	4.3 V
1/4	3.8 V	4.1 V	2.7 V
1/6	3.3 V	2.9 V	1.3 V
1/12	2.2 V	1.7 V	0.4 V
1/20	1.4 V	1.1 V	0.15 V

Figure 8. Dependence of the integral energy (G_{int}) of BF_4^- anions ($\bullet$) on the relative electrode potential squared (ΔU^2). Blank markers ($\circ$) indicate BF_4^- dissociation to $BF_3 + F^\cdot$. Surface coverage (θ) is labeled with arrows. The slope corresponds to the differential capacitance value of 6 $\mu F/cm^2$.

As it can be seen in Figure 9, at $\theta = 1/3$, the physical adsorption energy difference between the undissociated and the dissociated structures is relatively small (11 kJ/mol), while the potential difference is well pronounced (1.1 V). The adsorption energy results from the lateral repulsion among the species, which is not very sensitive to their orientation. On the opposite, the potential is directly related to the interfacial dipole moment, which is apparently determined by the orientation of species (BF_4^-, F^-, BF_3).

At high surface coverages $\theta \geq 1/3$ and electrode potentials $\Delta U \geq 3$ V, when a BF_4^- anion is flipped, it spontaneously dissociates to BF_3 and $F^\cdot$ (Figure 6b). As follows from Table 3, the total ionic charge on BF_4^- noticeably depends on the surface coverage, varying from $-0.7e$ to $-0.4e$. Hence, due to the strong inter-ionic repulsion, $-E_{ads}$ decreases with increasing θ (Figure 9). Differently, the charge on $F^\cdot$ is only slightly above $-0.4e$ at all coverages. Thus, in the absence of strong inter-ionic repulsion, $E_{ads}(F^\cdot)$ weakly depends on θ (Figure 9).
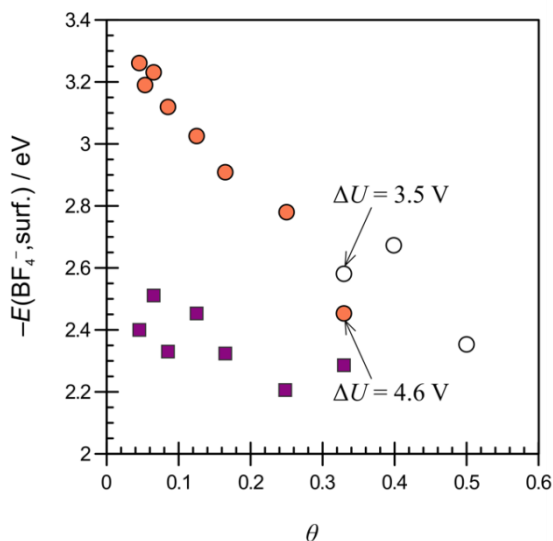
Figure 9. Dependence of the BF_4^- (●) and F^- (■) adsorption energies (E_{ads}) on the surface coverage. At high coverage, BF_4^- is oxidized and dissociates into BF_3 and $F^{\cdot}$ (○). Relative electrode potential (ΔU) is labeled with arrows.

Table 3. The values of the adsorption energy (E_{ads} / kJ mol^{-1}) for different surface coverages (θ) were evaluated from the results of calculations using RPBE and vdW-DF functionals. Ionic charges (q / e) were obtained using DDEC method [108,109], whereas the distance (d / Å) was calculated from the position of the nearest layer of Au nuclei to the layer of B nuclei.

Adsorbate	θ	$-E_{ads}$ / kJ mol^{-1}	$-q / e$	d / Å
BF_4^-	1/3	237	0.41	2.94
BF_4^-	1/4	268	0.41	2.99
BF_4^-	1/6	281	0.49	3.01
BF_4^-	1/12	301	0.62	3.11
BF_4^-	1/20	308	0.67	3.13
$F^{\cdot}(BF_3)$	1/3	248	0.36	
$F^{\cdot}$	1/3	221	0.34	
$F^{\cdot}$	1/4	213	0.34	
$F^{\cdot}$	1/6	224	0.37	
$F^{\cdot}$	1/12	225	0.38	
$F^{\cdot}$	1/20	232	0.39	

5.3.2 Relative electrode potential and integral capacitance

DFT calculations capture the oxidation process that sets the anodic limit on the electrochemical window for Au(111)–EMImBF$_4$ interface. Due to the simplicity of the Helmholtz model, the corresponding potential remains overestimated. Table 2 shows the potential values at the Au(111)–BF$_4^-$ interface calculated for different surface coverages using MD simulation assuming the Helmholtz (MD$_H$) in comparison with DFT calculations data. The computational MD and DFT results are in agreement with each other at $\theta < 1/3$. In the MD simulations, the spontaneous flip of anions takes place at $\theta = 2/5$ leading to the formation of the second layer of anions and crowding at the interfacial layer. At such high coverages, in the DFT calculations, BF$_4^-$ loses its charge and decomposes (Table 3). Besides that, both DFT and MD computations show that the distance of closest approach of BF$_4^-$ to the surface decreases with the increase of coverage as well as with the positive value of the surface charge (*i.e.* electrode potential). That is reflected by the slight increase of the integral capacitance, shown in Figure 10.
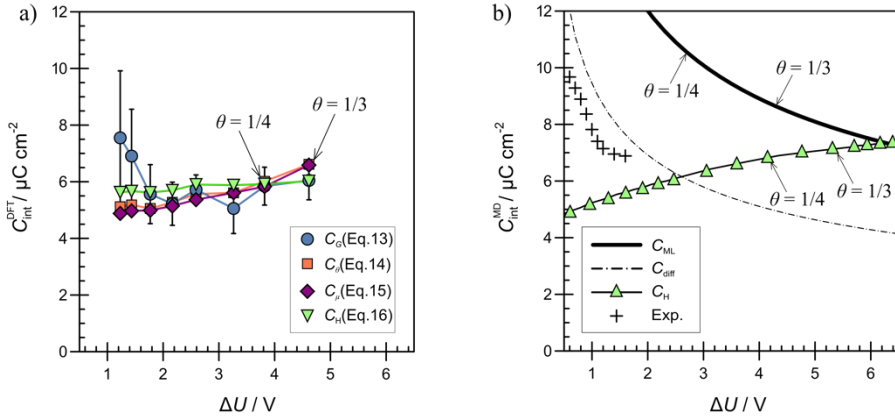
Figure 10. a) Dependence of integral capacitance on potential, calculated using the DFT data and Eqs. 13–16. b) Dependencies of integral (C_{ML} and C_H) and differential (C_{diff}) capacitance on potential calculated using the MD data. Surface coverage values (θ) are labeled with arrows. Experimental data have been taken from Ref. [111], where Au–EMImBF$_4$ interface was studied using electrochemical impedance spectroscopy.

Figure 10a shows the integral capacitance values calculated according to Eqs. 13–16 for the systems with all BF$_4^-$ ions in the same orientation, *i.e.*

characterised by the largest possible interfacial dipole moment. The match between the Eqs. 13–16 curves imply consistency in the mechanism and energetics: the accumulation of ions takes place via simple physical adsorption, and the integral energy rises due to repulsion between counter-ions.

The integral capacitance for the more complex, multilayer Au(111)–EMImBF$_4$ interface shows the impact of the ionic layering on the potential magnitude. In Figure 10b, at the same potential value, the capacitance calculated using multilayer model is higher than that calculated using Helmholtz model. At the same surface coverage (or surface charge) the relative electrode potential values are smaller for the multilayer model than for the Helmholtz model, as shown in Table 2. Only when the monolayer of counter-ions of maximal density is formed, the potential, surface charge, and integral capacitance are the same for both models. In our simulations, this takes place at the surface coverage of 2/5 and at the very high potential of 6.3 V. Above this value crowding of anions at electrode interface occurs.

The obtained capacitance values are in reasonable agreement with experimental high-frequency differential capacitance values from 5 to 10 $\mu F/cm^2$ measured at the gold single crystal (100) and (111) surfaces [57,58,68,71,84–86]. However, the capacitance calculated using Helmholtz model increases with increasing the relative electrode potential, while the capacitance calculated using interfacial multilayer model decreases in the same way as in experimental work [111].

5.3.3 Anionic adlayers *vs.* dense monolayer of anions

The presented results can be interpreted through theories developed by Loth *et al.*, Bazant–Storee–Kornyshev or Yochelis, as well as molecular-level interpretations by Feng *et al.* and Ivaništšev *et al.* [47,49,50,56,112]. According to Feng *et al.*, the multilayer structure can be divided into layers with zero net charge (except for the innermost layer) and characterised by alternating dipole moments from layer to layer [50]. The presence of the structured RTIL above the innermost layer decreases the absolute value of the potential drop across the interface. That is why in Figure 10 the integral capacitance for the multilayer model is higher than that for the Helmholtz model. According to Ivaništšev *et al.*, the capacitances are equal at the

potential of the monolayer formation when a single monolayer of counter ions completely compensates the surface charge [56]. These potentials manifest the transition from overscreening to crowding regimes [47,56,113]. At lower absolute electrode potentials, due to the anion–cation interaction correlation, there is an alternating layer of anions and cations; at higher absolute potentials, the surface is crowded by the counter-ions.

In the presented MD simulations, the potential of the monolayer formation was found to be at extremely high potential 6.3 V (Figure 10b, the cross point of C_{H} and C_{ML}), which corresponds to the coverage of 4/5 or 65 $\mu\mathrm{C/cm}^2$ (accounting for polarizability of ions). However, the DFT calculations demonstrated that the interface becomes unstable already at 3.5 V ($\theta = 1/3$, Figure 6b and Figure 9). In the hypothetical DFT based MD simulations of the multilayer model, the decomposition potential should be even lower, firstly, due to the dissociation of the oxidised BF_4^-, and, secondly, due to the ionic layering. In experiment, the anodic electro-chemical reactions started around 1.6 V *vs.* pzc [111].

Notice, that from a geometrical point of view the BF_4^- patterns at the coverage higher than 1/6 completely occupy the innermost layer, as the free space on the surface is sterically hindered for larger cations. In the MD simulations of the multilayer model, this coverage corresponds to 1.3 V (Table 2). It should be noted, that similar structures were visualized by the scanning tunnelling microscopy in Refs. [86,87], where the formation of the ordered anionic adlayers was assigned to low voltages of less than 1 V *vs.* pzc. In this case, the observation of the anionic adlayers does not rule out the overscreening nor the presence of $EMIm^+$ cations next to the innermost layer. Moreover, the accumulation of anions starting from the coverage of 1/6 and ending with the monolayer formation at coverage $\approx$ 4/5 requires marked potential and surface charge increase. Consequently, 1) anionic adlayers and the dense monolayer of anions are having different structures, 2) the adlayers are part of the multilayer EDL, and 3) the crowding of anions at low potential values is extremely improbable.

5.3.4 Helmholtz layer *vs.* Multilayer models

Comparison of the DFT and MD results provides a ground for resolving whether the EDL in RTILs at Au(111) is *one-* or *multi*-ionic-layer thick. According to Helmholtz model (Eq. 16), for the *one*-ionic-layer thick EDL, the capacitance is almost independent of the potential. For the multilayer model, both calculated integral and differential capacitances decrease with increasing the relative electrode potential (Figure 10b). The same tendency was shown for the differential capacitance of the Au–EMImBF$_4$ interface in the experiment [111]. Also, previous computations by Feng *et al.* [50] and Hu *et al.* [114] showed that while some qualitative trends might be captured by structural changes in the innermost layer, the subsequent layers have an essential influence in defining the dependence of capacitance on the electrode potential. All in all, the multilayer EDL structure in EMImBF$_4$, as a whole, determines the overall potential-dependent capacitance.

In the Helmholtz model, the EDL thickness is defined as the distance of closest approach of the counter-ions to the surface. Only for this model, the positions of the ionic charge and the ionic mass planes coincide. The first one position defines the potential drop in the corresponding parallel plate capacitor. The second effect appears due to steric interactions. Both effects might be equal to the counter-ion radius under an assumption that the surface charge plane lies at a surface-atom radius distance defined by the nuclei positions.

For the multilayer EDL structure, the ionic charge and mass plane positions are different. The ionic mass density is positive at any distance from the surface, while the sign of the ionic charge density (ρ) depends on the excess of anions or cations at a given distance from the surface (z). The ionic charge plane position (z_{ion}) is expressed as:

$$z_{\mathrm{ion}} = - \int \frac{\rho z(z)}{\sigma} dz \qquad (17)$$

z_{ion} value can be smaller than the counter-ion radii. On the contrary, in the multilayer structure, any *i*-th layer lies further from the surface than of the innermost layer.

Force–distance curves, as those provided in Refs. [75,115], can be used to count the number of layers and to estimate the geometrical thickness of the EDL. However, such thickness would be useless for calculating the EDL capacitance as the surface charge–potential dependence is dictated by the ionic charge plane position. To clarify the differences observed let us simplify the multilayer model into an ionic bilayer model.

5.3.5 Ionic bilayer model

In the recent ionic-bilayer model, the multilayer was presented as the contact layer of counter-ions and the subsequent layer of co-ions [116]. It is a simplified representation of the multilayer EDL. The integral and differential capacitances of this model are given as:

$$C = \frac{\varepsilon\varepsilon_0}{d - \delta\frac{\lambda}{\sigma}} \tag{18}$$

$$C_{\text{diff}} = \frac{\varepsilon\varepsilon_0}{d - \delta\frac{\mathrm{d}\lambda}{\mathrm{d}\sigma}} \tag{19}$$

where δ is the geometrical distance between the first and the second layers, ε is the high-frequency dielectric constant, and λ is the co-ion charge density in the second layer that is equal in magnitude, but opposite in sign to the surface charge excess of the counter-ions in the first layer [113].

Let us use this simple model to reflect the thickness of the EDL. Note, that the condition $\lambda = 0$ means that the model simplifies to the Helmholtz model. Otherwise, by definition, the EDL in the ionic-bilayer model is a two-layer structure with a geometrical width of $d + \delta$. Herewith, for the integral capacitance, the denominator in Eq. 18 is smaller than d. That is why the integral capacitance is higher in the simulations applying the multilayer model than values applying the Helmholtz model (Figure 10b). For the differential capacitance, the denominator in Eq. 19 might be equal to $d + \delta$ only when the surface charging relies solely on the exclusion of the co-ions from the second layer to the bulk, *i.e.* $\mathrm{d}\lambda = -\mathrm{d}\sigma$. The more traditional mechanism of charging implies adsorption of counter-ions on the

surface. Competition between these formation mechanisms ensures that the condition $d\lambda = -d\sigma$ is not satisfied. The change in the rate of the second layer destruction ($d\lambda/d\sigma \to -1$) causes the decrease of the capacitance with increasing the potential after a maximal co-ion charge density is accumulated in the second layer when $d\lambda/d\sigma = 0$ [116]. From Figure 10b one can deduce that this occurs at around 2.6 V, *i.e.* at an intersection of C_H and C_{diff}. Note, the capacitance decreases with increasing potential also at lower potentials. According to Eq. 19, the capacitance peak (not shown in Figure 10b) appears at potential when the accumulation of co-ions is maximal ($d\lambda/d\sigma \to d/\delta$), and the capacitance inevitably decreases above this potential. Most important for our discussion is that the geometric thickness of the ionic bilayer model is unrelated to its capacitance *vs.* potential dependence.

In the case of multilayer EDL model, one should account at least for two layers in the geometrical interpretation of the potential-dependent capacitance. The knowledge of the pzc position is essential. It allows for using both Eqs. 18 and 19 by converting the differential capacitance to the integral capacitance or calculation of the surface charge *vs.* potential dependence. In principle, one can estimate δ, λ, and $d\lambda/d\sigma$ values, among which only δ has a geometric meaning. The general hypothesis is that the ionic charge plane position could be estimated by accounting for two ionic layers, as in the ionic bilayer model [116]. Substituting the *one*-ionic-layer thick foundation of the Helmholtz model with a *multi*-ionic-layer one is a step towards a more general model of the EDL in RTILs.

5.4 Conclusive remarks

The adsorption of BF_4^- anions from $EMImBF_4$ on the charged Au(111) surface has been studied using DFT and MD computations. The study represents a crucial piece of the scientific puzzle. It addresses the question: is the innermost layer dominate in the overall potential-dependent multilayer EDL? It also illustrates how the interfacial dipole conception is set up.

First, DFT calculations and MD simulations of the simplest Helmholtz layer model of the Au(111)–BF_4^- interface give similar results, once a surface change plane position is adjusted in the MD simulations. This adjust-

ment introduces a correction of the surface dipole to the so-called ionic dipole. As expected, the Helmholtz capacitance is almost independent of the potential. Second, in the MD simulations of the multilayer model of the polarised Au(111)–EMImBF$_4$ interface, the interfacial dipole is significantly reduced due to the ionic layers above the innermost layer. The latter represents a solvent dipole, *i.e.,* a contribution from the EDL ions except for those counter-ions that compensate the surface charge. For the multilayer EDL model, the capacitance is dependent on the potential, in-line with the experimental results [111]. Both solvent and surface dipoles are crucial components of the total interfacial dipole as well as of the potential drop.

We concluded that the multilayer EDL in EMImBF$_4$, as a whole, determines the overall potential-dependent capacitance. We introduce an ionic bilayer model that accounts for the dipole formed due to the adsorption of counter-ions as well as for the dipole formed due to anion–cation interplay.

6. ELECTRICAL DOUBLE LAYER AT CIRCUMCORONENE–IONIC LIQUID INTERFACE

Graphene has a unique set of properties, such as high electrical and thermal conductivity, high specific surface area, flexibility and optical transparency. These properties are utilized in novel energy conversion and energy storage devices. In complement to experiment and theory, computer simulation helps to find links between the chemical structure of the graphene interfaces and their performance in energy conversion and energy storage applications. Application of theoretical methods for analysis of the electronic structure of graphene-like materials is beneficial for both understanding of the interfacial interactions as well as assisting in the development of new applications [117].

Understanding the interaction of RTILs with carbon materials is crucial in the development of batteries and supercapacitors, CO_2 capture-and-storage devices, superconducting devices and electromechanical systems [118,119]. Non-periodic models containing ionic associates at polyaromatic hydrocarbons taken as model surfaces are used to study the various surface phenomena taking place at the carbon–electrolyte interfaces [120–122]. The partial charge transfer process between graphene model surface and adsorbed ions are an essential feature of these systems [122]. Although it can be estimated with the DFT, the predicted transfer degree depends on the calculation method, partially, due to the self-interaction error (SIE) [123].

Circumcoronene represents a model of carbon surface and has a chemical formula – $C_{54}H_{18}$. In this part, the partial charge transfer at a model carbon surface–electrolyte interface (consisting of a circumcoronene and RTIL ionic pairs) has been evaluated.

6.1 Literature overview

Only in a few studies of ILs, the SIE effect on the DFT calculations was examined [98,124,125]. Grimme *et al.* concluded that the SIE error is almost negligible for three studied ionic pairs [124]. For a larger set of ionic associates, Lage-Estebanez *et al.* showed that the SIE is pronounced in the

case of specific combinations of ions, in particular for ionic pairs including halide anions and/or pyridinium cation [98,126]. Similar studies of a large set of organic molecules and halide ions indicated that the SIE is notable [127–129]. Its effect was observable in terms of partial charge transfer between atoms/ions and carbon surface [122].

Polyaromatic hydrocarbons represent a class of carbon materials that are intermediate between graphene and porous carbons. Currently, they are among the most studied organic semiconductors due to the appealing characteristics of their electronic structure [130,131]. A wide variety of materials containing aromatic hydrocarbons are used in batteries because carbon-containing structures exhibit both higher specific charges and more negative redox potentials than most of the metal oxides and chalcogenides [132]. Wherein, the partial charge transfer process between the adsorbing ions and the electrode surface may become a useful phenomenon affecting the electronic properties of the interface, especially in the case of supercon-ductors [133].

The partial charge transfer from an adsorbate to a model carbon surface depends on the model size and structure. In computations, it also depends on the methods used for calculations and analysis. Baker and Head-Gordon observed that DFT methods overestimate the charge transfer due to the SIE, whereas Hartree–Fock (HF) method underestimates charge transfer process due to overlocalization [122].

To investigate the effect of the SIE on the DFT calculations involving ILs, two sets of imidazolium-based ionic pairs were selected: $[EMIm^+][BF_4^-,$ $PF_6^-, AlCl_4^-]$ and $[EMIm^+][Cl^-, Br^-, I^-]$. The latter set consists of ionic pairs that are strongly affected by the SIE [98]. The corresponding ILs are commonly used in experimental as well as computational studies [65,113, 134–145]. For example, an electrolyte containing $AlCl_4^-$ anions was pro-posed for ultrafast rechargeable aluminium-ion battery [134,135]. Very high energy density and power density values were achieved for supercapacitors using $EMImBF_4$, $LiPF_6$ or $NaPF_6$ based electrolytes [136–138]. A noticeable increase in power density (~20–30%) and shorter charging-discharging times were demonstrated for supercapacitors based on mixed ILs [136]: $EMImBF_4 + EMImI$, $EMImBF_4 + EMImBr$, $EMImBF_4 + EMImCl$. These ILs

are also demonstrating reversible specific adsorption with partial charge transfer effect at metal as well as at highly oriented pyrolytic graphite surfaces [65,139–142].

6.2 Computational methods

The effect of the SIE was analysed based on adsorption data for six ionic pairs at the molecular model of graphene – circumcoronene ($C_{54}H_{18}$). Such relatively small non-periodic systems are suitable for calculations with hybrid functionals that alleviate the SIE. The ionic pairs consisted of 1-ethyl-3-methylimidazolium = $EMIm^+$ cation and chloride = Cl^-, bromide = Br^-, iodine = I^-, tetrafluoroborate = BF_4^-, hexafluorophosphate = PF_6^- or tetra-chloroaluminate = $AlCl_4^-$ anions. The geometry of an ionic pair on top of fixed circumcoronene (as given in Figure 11) was optimised starting from a typical π-stacking distance of 3.5 Å between the imidazolium ring and the electrode surface plane. All following single point calculations were performed based on optimised geometries.
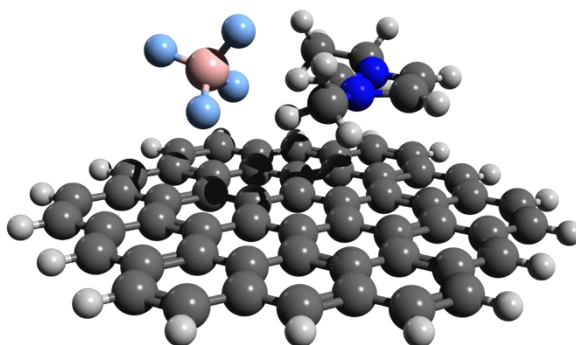
Figure 11. Optimised $C_{54}H_{18}$–$EMImBF_4$ structure. The figure was prepared using Avogadro software [146].

All DFT calculations were run using the ORCA 4.0.0 program [147] using Perdew–Burke–Ernzerhof (PBE) [148] functional and its reparametrised version (PBEh-3c) [149]. The optimisation was conducted with the PBEh-3c method using double-ζ basis set (def2-mSVP), Grimme's dispersion correction (D3) [150,151], and geometrical counterpoise correction (gCP) [152].

More detailed information regarding PBEh-3c optimisation methodology can be found in Ref. [153].

The Charges from Electrostatic Potentials using Grid-based method (ChelpG) [154] was used for the estimation of charges at circumcoronene–ionic pair interface. Interaction energy E_{int}, adsorption energy E_{ads} and dissociation energy E_{diss} were calculated to describe the processes depicted in Figure 12.

Figure 12. Processes occurring between ions of ionic liquid on the circumcoronene surface and away from it. The geometries of single ions and ionic pairs in vacuum were fixed and identical to the optimised geometries at the circumcoronene surface.
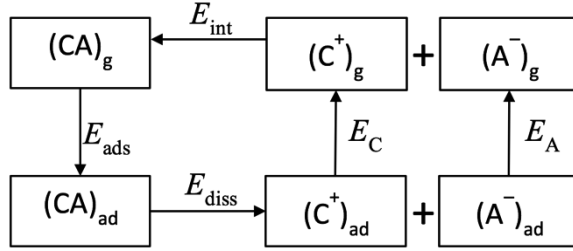
The interaction energies of ions in the solution, ΔE_{int}, were defined as the difference between the energy of the ionic pair (CA), cation (C), and anion (A):

$$\Delta E_{\text{int}} = E(\text{CA}) - E(\text{C}) - E(\text{A}) \tag{20}$$

The adsorption energy ΔE_{ads} was defined as the difference between the energies of the circumcoronene–ionic pair associate ($E(\text{C}_{54}\text{H}_{18}\text{–CA})$), ionic pair (CA), and circumcoronene ($\text{C}_{54}\text{H}_{18}$):

$$\Delta E_{\text{ads}} = E(\text{C}_{54}\text{H}_{18} - \text{CA}) - E(\text{CA}) - E(\text{C}_{54}\text{H}_{18}) \tag{21}$$

The dissociation energy of an IL associate on the circumcoronene surface ΔE_{diss} was defined as the difference between the sum of the energies of circumcoronene ($\text{C}_{54}\text{H}_{18}$) and the circumcoronene–ionic pair associate ($E(\text{C}_{54}\text{H}_{18}\text{–CA})$), subtracting the energies of the circumcoronene–cation ($\text{C}_{54}\text{H}_{18}\text{–C}$), and circumcoronene-anion ($\text{C}_{54}\text{H}_{18}\text{–A}$):

$$\Delta E_{\text{diss}} = E(\text{C}_{54}\text{H}_{18} - \text{CA}) + E(\text{C}_{54}\text{H}_{18}) - \\ -(\text{C}_{54}\text{H}_{18} - \text{C}) - E(\text{C}_{54}\text{H}_{18} - \text{A}) \tag{22}$$

According to the diagram in Figure 12, the sum of desorption energies of individual anion and cation from the circumcoronene can be expressed through ΔE_{int}, ΔE_{ads}, ΔE_{diss} as:

$$E_{\text{A}} + E_{\text{C}} = \Delta E_{\text{diss}} - \Delta E_{\text{ads}} + \Delta E_{\text{int}} \tag{23}$$

6.3 Computational results

6.3.1 Adsorption, interaction and dissociation energies

Table 4 presents calculated adsorption (E_{ads}), interaction (E_{int}), and dissociation (E_{diss}) energies. E_{ads} decreases in a row: $\text{EMImPF}_6 \approx \text{EMImAlCl}_4 > \text{EMImBF}_4 > \text{EMImCl} \approx \text{EMImBr} \approx \text{EMImI}$, and the dispersion contributes to one-half of the adsorption energy. For E_{int} and E_{diss} the situation is opposite – in the absence of the surface, the contribution of dispersion forces is relatively low. As expected, comparison of E_{int} and E_{diss} shows that the dissociation of an ionic pair at the circumcoronene requires less energy than in vacuum.

According to Eq. 23, the sum of E_{ads}, E_{int}, and E_{diss} equals to the desorption energies of individual anion and cation (E_{A} and E_{C}). E_{A} and E_{C} values were calculated for the optimised associate geometry by removing the counter-ion and assigning the charge. Apparently, the cation interacts with the surface much stronger than any of the anions. $E_{\text{C}} \approx 119$ kJ/mol for all associates has been obtained. The desorption energy of anions (in kJ/mol) decreases in a row: Cl^- (37.8) > PF_6^- (19.8) ~ Br^- (16.1) ~ BF_4^- (14.8) ~ AlCl_4^- (10.2) > I^- (3.4). The row presents an interesting contradiction: it is known from experiments, the iodide is taken as a strongly adsorbing anion.

Table 4. Energies of ionic pair adsorption on circumcoronene (E_{ads}), anion–cation interaction (E_{int}) and ionic dissociation at the circumcoronene surface (E_{diss}). All values are calculated with the PBEh-3c functional and are given in kJ/mol. D3 denotes the Grimme's dispersion correction.

Ionic pairs	E_{ads}		E_{int}		E_{diss}	
	E_{ads}	D3	E_{int}	D3	E_{diss}	D3
EMImCl	−81.6	−45.6	−465.6	−4.2	390.9	−3.7
EMImBr	−79.0	−46.4	−401.0	−4.2	346.1	−3.7
EMImI	−79.2	−47.3	−363.3	−4.6	321.1	−4.1
EMImBF$_4$	−85.0	−47.8	−367.0	−6.0	318.6	−5.3
EMImPF$_6$	−96.4	−53.4	−344.0	−7.6	301.7	−6.8
EMImAlCl$_4$	−95.3	−54.1	−330.2	−11.1	295.2	−10.3

As shown in Table 5 the energetic values of PBE are different from PBEh-3c. Interestingly, the total energies are almost the same, but the contribution of the dispersion effect is very different. That is due to the different redistribution of charges in the systems, as discussed below. The contribution of geometrical counterpoise correction is not significant in both methods used.

Table 5. Circumcoronene–ionic pair adsorption energies (E_{ads}) with Grimme's dispersion (D3) and geometrical counterpoise (gCP) corrections calculated using two different functionals: PBE and PBEh-3c. (Values are given in kJ/mol)

Ionic pairs	PBE			PBEh-3c		
	E_{ads}	D3	gCP	E_{ads}	D3	gCP
EMImCl	−81.7	−71.3	2.5	−81.6	−45.6	5.3
EMImBr	−80.5	−72.4	3.3	−79.0	−46.4	5.7
EMImI	−83.4	−75.2	3.0	−79.2	−47.3	5.4
EMImBF$_4$	−84.7	−73.6	3.9	−85.0	−47.8	7.9
EMImPF$_6$	−94.7	−75.2	3.0	−96.4	−53.5	9.0
EMImAlCl$_4$	−95.7	−85.4	2.8	−95.3	−54.1	5.4

6.3.2 Specific adsorption of ions

Specific adsorption of ions from ILs on carbon materials plays a vital role in various electrochemical phenomena and produces a significant effect on the equilibrium parameters of the interphase boundary and the rate of electrochemical processes [155–157]. Recently, much attention has been dedicated to adsorption of halide anions because the presence of specifically adsorbing halide anions leads to the increase of interfacial capacitance and, therefore, the energy density of supercapacitors [140,158,159].

To understand what may lead to specific adsorption, we performed a computational study of the adsorption of a single anion on neutral surface of $C_{54}H_{18}$ ($C_{54}H_{18} + A^- \rightarrow C_{54}H_{18}$–$A^-$) and at charged circumcoronene ($C_{54}H_{18}^+$ + $A^- \rightarrow C_{54}H_{18}^{\delta+}$–$A^{\delta-}$). Table 6 shows the energies and charges for these two interfaces. In general, at the neutral surface, bromide and iodide show very lower tendency to adsorb (lower absolute E_A values). It is worth mentioning that in calculations the minus charge of the $C_{54}H_{18}$–A^- system is localised on the anion. The situation changes when the surface is polarised. Then the absolute charge of halide anions decreases almost to zero. The halide anions transfer their charge to the surface. It is worth noting, how the E_A changes when one electron is removed from the system. For the molecular anions, the adsorption becomes more favourable due to the Coulomb attraction between the charged surface and the adsorbed anions. In the case of halide anions, the adsorption becomes even more favourable due to the circumcoronene–halide covalent bonding. Interestingly, at positive surface charge densities, anions adsorb more strongly than EMIm$^+$ cation at negative surface charge density. Although with the neutral surface the adsorbed cations interact much stronger than any of the anions.

Table 6. Adsorption energies (E) and absolute charges (q) of single anions (A) and cation (C) on neutral ($C_{54}H_{18}$) and charged ($C_{54}H_{18}^{+/-}$) circumcoronene. Energies are calculated with the PBEh-3c functional and are given in kJ/mol, charges are calculated with ChelpG and values are presented in e.

Anion	$C_{54}H_{18}-A^-$		$C_{54}H_{18}^+-A^-$	
	E_A	q_A	E_A	q_A
Cl⁻	−40.9	−0.75	−377	−0.03
Br⁻	−16.9	−0.81	−345	−0.10
I⁻	−3.25	−0.84	−331	−0.03
BF$_4^-$	−30.8	−0.76	−256	−0.73
PF$_6^-$	−26.2	−0.78	−242	−0.75
AlCl$_4^-$	−24.0	−0.82	−234	−0.79
Cation	$C_{54}H_{18}-C^+$		$C_{54}H_{18}^--C^+$	
	E_C	q_C	E_C	q_C
EMIm⁺	−122	0.77	−205	0.74

Table 7 shows the total dipole moment of the studied systems in the direction perpendicular to the circumcoronene surface plane. The dipole originates from the specific arrangement of anions and cations on the charged surface. The dipole is also affected by the partial charge transfer process between an ionic pair and circumcoronene. As expected, different DFT methods give a distinct estimation of the partial charge transfer step. Both PBE and PBEh-3c show the similar trend. In the context of the interfacial potential drop ($\Delta\varphi$), the latter is proportional to the interfacial dipole moment (μ) as $\Delta\varphi \sim \mu$.

Different types of ions contribute to the interfacial dipole formed, obviously, to a variable extent. It might be speculated that at a given surface charge density the adsorption of halide anions from EMImBF$_4$+EMImX mixtures would decrease the potential drop relative to its value in the pure EMImBF$_4$ ionic liquid, as observed in experiments [139,141,158]. Thus, the capacitance for $C_{54}H_{18}$–EMImBF$_4$+EMImX systems would decrease for halide anions in a row: I⁻ > Br⁻ > Cl⁻. Such simple estimation is in line with the experimental findings [160–162].

Table 7. Dipole moment values (in Debye).

	PBE	PBEh-3c
$C_{54}H_{18}$–EMImCl	−0.06	−0.39
$C_{54}H_{18}$–EMImBr	+0.23	+0.01
$C_{54}H_{18}$–EMImI	+0.57	+0.56
$C_{54}H_{18}$–EMImBF$_4$	−0.80	−0.53
$C_{54}H_{18}$–EMImPF$_6$	−1.08	−0.78
$C_{54}H_{18}$–EMImAlCl$_4$	−2.22	−2.11

6.3.3 Charge distribution analysis

Within the generalized gradient approximation (GGA), an ionic pair CA may dissociate into spurious fractional charge fragments $C^{\delta+}$ and $A^{\delta-}$, with an energy that is lower than of C^0 and A^0, if the lowest unoccupied orbital energy of anion (A) lies below the highest occupied orbital energy of the cation (C). The spurious fractional charge dissociation arises from the SIE – the failure of being exact for all one-electron densities is inherent for all the semilocal functionals. The SIE manifests itself most clearly in the long-range region of the interaction energy curve for diatomic associates as well as even at optimal distances for the large carbon surface model–alkali metal associates [122,163]. There are different ways to suppress the SIE, including utilisation of hybrid functionals, such as B3LYP, M06-2X, and PBEh-3c.

The difference between using PBE and PBEh-3c functionals can be seen in the absolute charge values (Table 8). The charges (in absolute scale) obtained with the PBEh-3c functional are higher than those obtained with the PBE functional. The absolute partial charges show two sets of anions: halide anions with smaller charges, and multiple atoms anions (BF_4^-, PF_6^-, $AlCl_4^-$) with more significant charges. The PBEh-3c functional, where SIE is taken into account compared to PBE, decreases the partial charge transfer, which is most pronounced for the halide anions.

Table 8. The absolute charge of the anion (calculated with ChelpG, values in *e*).

Ionic pair	PBE		PBEh-3c	
	q_{CA}	$q_{C54H18-CA}$	q_{CA}	$q_{C54H18-CA}$
EMImCl	−0.70	−0.63	−0.73	−0.66
EMImBr	−0.71	−0.65	−0.76	−0.71
EMImI	−0.70	−0.64	−0.78	−0.75
EMImBF$_4$	−0.87	−0.75	−0.87	−0.78
EMImPF$_6$	−0.89	−0.78	−0.89	−0.80
EMImAlCl$_4$	−0.79	−0.75	−0.84	−0.82

Table 9 shows the electronic charge redistribution calculated. The most prominent charge distribution occurs for AlCl$_4^-$ anion containing ionic pair on the circumcoronene surface, while for other systems the surface charge distribution is unnoticeable. The utilisation of the PBEh-3c functional lowers partial charge transfer values between anion and cation. Our results show smaller changes for the cations and less variation in the charge difference for anions. Note that the difference between charge densities calculated using PBE and PBEh-3c for the Δq_{C54H18} is within the limits of computational error. The partial charge transfer between the circumcoronene surface and adsorbed ionic pairs is insignificant. However, the inter-ionic charge redistribution is pronounced and is sensitive to the calculation method used.

Table 9. Charge difference values (calculated with ChelpG, values in e).

Ionic pair	PBE			PBEh-3c		
	Δq_{C54H18}	Δq_A	Δq_C	Δq_{C54H18}	Δq_A	Δq_C
EMImCl	−0.006	−0.066	0.073	0.012	−0.068	0.056
EMImBr	−0.013	−0.061	0.074	0.002	−0.051	0.049
EMImI	−0.017	−0.057	0.074	−0.013	−0.037	0.049
EMImBF$_4$	−0.020	−0.117	0.137	0.003	−0.089	0.086
EMImPF$_6$	−0.024	−0.112	0.136	0.007	−0.093	0.086
EMImAlCl$_4$	−0.043	−0.046	0.088	−0.031	−0.022	0.054

6.4 Conclusive remarks

A carbon–electrolyte interface was studied using a sophisticated PBEh-3c method and a simple model (circumcoronene–ionic pair). We focused on the analysis of the partial charge transfer phenomena.

1) At the neutral surface, the circumcoronene–ionic pair interaction leads only to a very minimal change in the circumcoronene atomic charge values. The estimated partial charge transfer values are different for PBE and hybrid PBEh-3c functionals, however, the absolute values are within the estimation errors. The electronic polarization effect at neutral interfaces might be neglected, even for halide anions.

2) At the charged surface, the covalent bond between circumcoronene and halide anions was observed, and this means that the specific adsorption takes place.

3) At the charged surface, for halide anions, the interaction becomes much stronger than for the physically (*i.e.* non-specifically adsorbed) anions due to the circumcoronene–halide anion covalent bonding. In the context of the thesis, the conclusions should read as that the covalent bonding significantly reduces the interfacial dipole value as well as the potential drop at electrode–electrolyte interface, thus leading to the capacitance increase at the interface.

7. THE BEHAVIOR OF RTILS ASSOCIATES AT METAL SURFACE UNDER APPLIED FIELD

The ion–ion correlation causes the characteristic layering at the interface between an electrode and a RTIL. An ionic pair counts only for a single cation–anion attraction. A monolayer of counter-ions includes only repulsive interactions between ions of the same charge. Larger associates of mixed composition account for both repulsive and attractive interactions between ions. Among symmetric associates, one the simplest is the one that contains three 1-ethyl-3-methyl imidazolium cations and three tetrafluoroborate anions [164] We conducted DFT calculations of such associate adsorbed at Au(111), Bi(111) and $C_{54}H_{18}$ surface (Figure 13) with a focus on the interfacial geometry and interaction strength under an applied field.
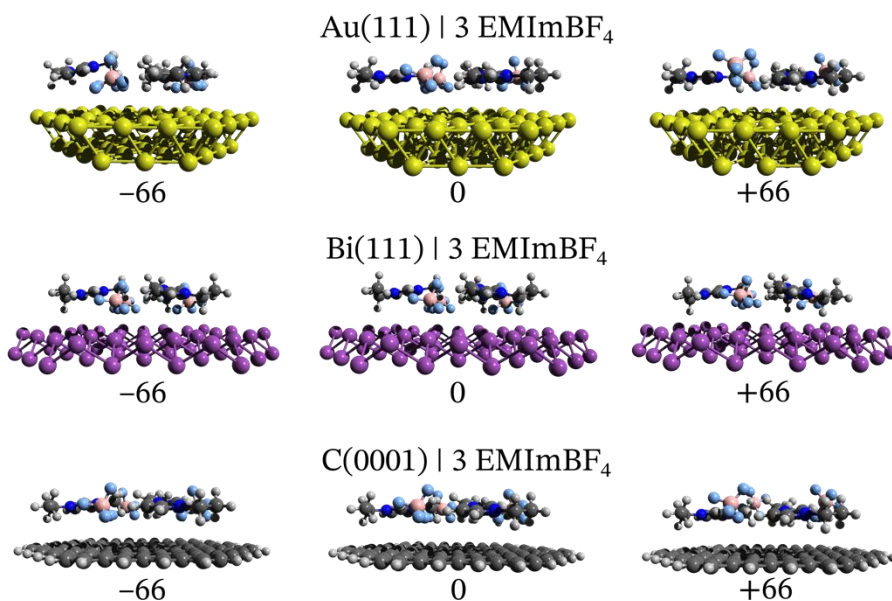

Figure 13. Geometries of the ionic associates at the applied field values: −66, 0 and +66 a.u. at Au(111), Bi(111), and $C_{54}H_{18}$ surfaces from top to bottom, respectively.

7.1 Computational methodology

DFT calculations were performed within the meta-GGA, using Minnesota Local functional (M06L) and the Ahlrics style split valence polarization basis set (Def2-SVP) as implemented in the Gaussian 09 program [26]. Calculations were performed on three rigid surfaces: at a two-layer Au(111) cluster, at a two-layer Bi(111) cluster, and at the $C_{54}H_{18}$ molecule. An associate of three $EMIm^+$ cations and three BF_4^- anions was placed on top of each cluster, and the geomtery of the structure was optimized under the applied field (F).

The interfacial binding energy (ΔE_{int}) is defined as the energy gain in the formation of the interface from the surface and $EMImBF_4$, and was calculated as follows:

$$\Delta E_{int} = E_{surface\text{-}EMImBF_4} - E_{surface} - E_{EMImBF_4} \qquad (24)$$

where E denotes the total energy of the chemical structure, which depends on the geometry, orientation and the applied electric field. The electric field was treated through finite-field DFT method implemented in the Gaussian program suite [26]. The values of the field in a direction normal to the surface were chosen so to specify a range for surface charge density (σ) between -6 and $+6\,\mu C\,cm^{-2}$:

$$F = \sigma/\varepsilon_0 \qquad (25)$$

7.2 Computational results

7.2.1 Structure changes

Figure 14 shows distances from top atom layer of three studied surfaces to the closest nitrogen atom of cations and boron atom of anions. The distance from the surface to cations increases in the row: $C_{54}H_{18}$ < Au(111) < Bi(111), but in case of anions the dependence is inverse. It is well evident that desorption of BF_4^- anion starts with decrease of surface charge density for all three of surfaces studied. The distance from $EMIm^+$ cation to the surface only slightly increases on Au(111) and $C_{54}H_{18}$ surfaces with increase of

surface charge density. As described in Chapter 6, $EMIm^+$ interacts more strongly with the neutral circumcoronene surface than anions. The same tendency also applies to the associate of $EMIm^+$ and BF_4^-.

The situation with the $EMImBF_4$ interfacial structure somehow resembles the interfacial H_2O network. In ice, each molecule shares four H-bonds. There are fewer H-bonds in liquid water then at the interaface, where at least one bond is broken in favor of the direct surface–H_2O interactions. In the $EMImBF_4$ crystal, each ion is surrounded by four counter-ions. The number of counter-ions is lower in the ionic liquid, and at least one counter-ion is replaced from the coordination shell in the vicinity of a surface. In our models, the coordination shell includes two counter-ions. In a periodic model, there can be precisely three counter-ions in a monolayer. A variable number of counter-ions can be accounted in the fully atomistic simulations, as presented in Chapter 5. The associate model is a trade of between accuracy and complexity. It shows that the anions and cations interchange upon charging the surface. However, it is restricted to keep the number of ions constant, while in the more complex MD simulations the desorption of the ions leads to the change in their number density profiles at the electrode surface.
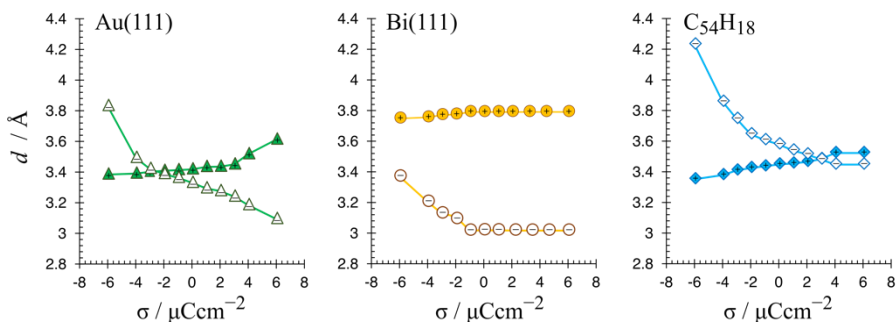

Figure 14. Distances (d) from top atom layer of Au(111), Bi(111) and $C_{54}H_{18}$ surfaces to the closest nitrogen atom of cations (filled markers) and boron atom of anions (transparent markers) of $EMImBF_4$ associates, represented as dependence on the electrode surface charge density.

7.2.2 Interaction energy and charge analysis

Figure 15 shows the dependence of interaction energy on the surface charge density. The interaction energy (per ionic pair) consists of the specific binding strength of anion and cation to the surface. On the Au(111) surface the ions are more strongly bond to the surface than on the Bi(111) and $C_{54}H_{18}$ surfaces. The Au(111)–EMImBF$_4$ cluster breaks at high surface charge density values due to the breakage of the anion–cation correlation as a result of the preferential adsorption of the counter-ions and Coulomb repulsion of the co-ions.
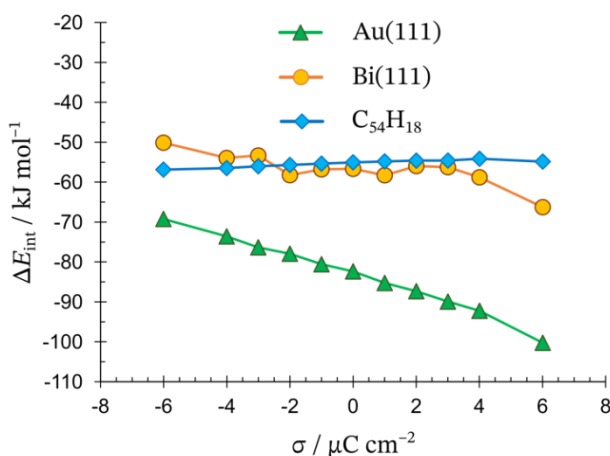

Figure 15. Dependence of interaction energy on the surface charge density.

Table 10 shows interaction energies in comparison with the results calculated and discussed in Chapters 5 and 6. First of all, it is worth paying attention to the adsorption of BF_4^- anion on the gold surface, which differs for cluster and periodic models [92]. Periodic calculations were performed at the charged surface, thus cannot be directly compared to the calculations at neutral clusters. Both types of calculation results are in a good agreement with Mertens *et al.* work [165], where authors performed calculations using gradient corrected functional for different charge state values, including the neutral cluster consisting of 39 atoms. Even better correspondence of calculated results with less advanced calculations can be found in the case of data obtained on bismuth. Siinor *et al.* [17] also performed an investigation of the

influence of cation chemical composition and structure on the adsorption parameters on the Bi(111)–EMImBF$_4$ interface using B3LYP functional. They found that interaction energy with the neutral metal cluster is stronger for BF$_4^-$ anion than for cation by 50 kJ/mol. Our calculations show a small difference, probably, due to the difference between B3LYP and M06L functionals. In case of C$_{54}$H$_{18}$, we can compare the M06L results with the values from Chapter 6 [153] that were obtained using PBEh-3c functional. Energy values are in good agreement with each other (both for the ion pair and for the individual ions interaction with the surface).

Table 10. Interaction energy values for four different cases at zero surface charge density. M06L results are marked with *. In work [92] RPBE+vdW functional was used, in work [17] B3LYP functional was used and in work [153] PBEh-3c functional was used.

Studied surface	Interaction energy (kJ mol^{-1}) between surface and			
	IL associate (per one ionic pair)	IL single ionic pair	anion	cation
Au(111)*	−82	−111	−124	−106
Au [92]			−227	
Au$_{39}$ [165]	−52			
Bi(111)*	−57	−49	−74	−70
Bi(111) [17]		−62	−90	−40
C$_{54}$H$_{18}$*	−55	−66	−35	−103
C$_{54}$H$_{18}$ [153]		−85	−31	−122

Partial atomic charges are useful descriptors for interpretation of the DFT results in a chemically intuitive fashion. It comes down to the description of the electron charge distribution within molecules through assigning a partial charge to each atom of the molecules. Because partial atomic charges are not physical observables and there is no strict quantum mechanical definition of them, many different models have been proposed to extract partial atomic charges based on the molecular charge distribution data. The Mulliken population analysis [166] and the natural population analysis (NPA) [167,168] are typical examples of proposed models which are based on partitioning the molecular wave function into atomic contributions in

terms of basis functions used to construct this wave function. The Mulliken population analysis is probably the best known of all models for distribution analysis of partial atomic charges. Due to its simplicity, this model is actively employed in computational chemistry. However, its results tend to vary with the basis set employed and obtained results are unrealistic in some cases [169]. These drawbacks partially arise from the fact that the Mulliken population analysis utilizes a non-orthogonal basis set. This problem is resolved in the NPA in which orthonormal natural atomic functions are used. In Figure 16a the dependence of NPA charges on the surface charge density is presented. The partial charge transfer process (per ionic pair) in NPA is pronounced for the Au(111)–3EMImBF$_4$ model and is neglectable for Bi(111)–3EMImBF$_4$ and C$_{54}$H$_{18}$–3EMImBF$_4$ models.
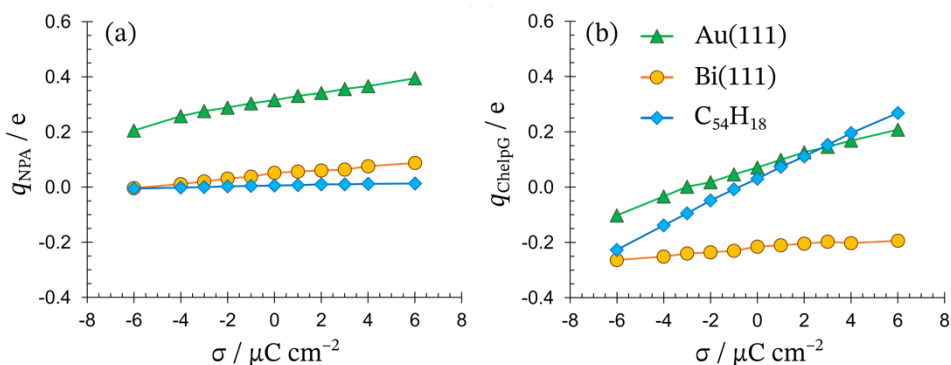

Figure 16. Dependence of (a) NPA charge transfer and (b) ChelpG charge transfer values on the surface charge density.

In its turn, ChelpG electrostatic potential-derived charges [154] allocate point charges to fit the computed electrostatic potential at a number of points at the molecular van der Waals surface. ChelpG charge values calculated per one ionic pair are presented in Figure 16b. ChelpG method indicates that the partial charge transfer is more sensitive to the surface charge Au(111)–3EMImBF$_4$ model and C$_{54}$H$_{18}$–3EMImBF$_4$ models selected than in case of Bi(111)–3EMImBF$_4$ system. Comparison of ChelpG charge values calculated seperately for anion and cation on the C$_{54}$H$_{18}$ surface with values from Chapter 6 shows that excellent agreement between this two computational works (Table 11) has been observed.

Table 11. ChelpG charge values for anion and cation at zero surface charge density.

Studied surface	ChelpG charge / e	
	BF_4^-	$EMIm^+$
$C_{54}H_{18}$	−0.74	−0.72
$C_{54}H_{18}$ [153]	−0.76	−0.77

7.2.3 Dipole moment analysis

Figure 17 presents the dependence of dipole moment (μ) on the surface charge density. The dipole perpendicular to the surface plane forms due to the partial charge transfer between the ionic cluster and the surface as well as due to the specific arrangement of anions and cations in the ionic cluster. As was shown in Chapter 5 it contributes to the potential drop across the interface, where $\mu_{total} = \mu_{ion} + \mu_{el} + \mu_{solv}$.
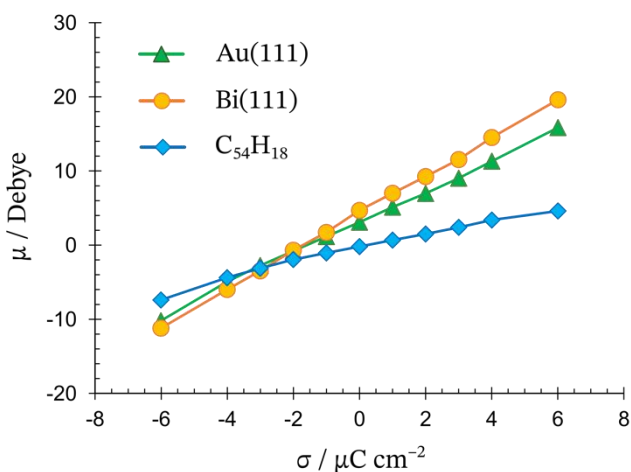

Figure 17. Dependence of the dipole moment perpendicular to the surface plane on the surface charge density for interfaces given in Figure 13.

The interfacial dipole may be split into three different dipole contributions for both (metallic and semimetallic) types of interfaces. The electronic dipole (μ_{el}) accounts for partial charge transfer as an extreme type of polarization. The solvent layer dipole (μ_{solv}) is responsible for the characteristic form of the differential capacitance on the electrode potential applied. The ionic

dipole (μ_{ion}) alone corresponds to the Helmholtz model. The latter neglects fluctuation of the electronic density at the metal (quantum effects) as well as the solvation of the surface. This effect has a similar effect as the partial charge transfer – reduces the magnitude of the interfacial dipole, *i.e.* the potential drop. In other words, the given surface charge can be accumulated at a lower energy cost. Table 12 represents interfacial dipole contributions for three studied interfaces at negative and positive surface charge densities. The prime implies that we assume that each ion holds a unit charge (1e and that $\varepsilon_r = 1$). The $\mu_{el} + \mu_{solv}$ dipole was calculated for interfaces noted in Figure 13, whereas $\mu_{ion} + \mu_{el}$ dipole was calculated for interfaces containing one ion on the surface. Both were taken from the computational output for z-direction. The $\mu_{ion} + \mu_{el}$ data were interpolated within ± 3 μC/cm^2 where the μ *vs.* σ dependence is linear. Note, at $\sigma > 6$ μC/cm^2 the modelled cluster starts to break.

Table 12. Calculated dipole moment values (in Debye) for different interfaces at negative and positive surface charge densities.

Studied interface	$\sigma = -3$ μC/cm^2			$\sigma = +3$ μC/cm^2		
	μ_{ion}	μ_{el}	μ_{solv}	μ_{ion}	μ_{el}	μ_{solv}
Au(111)–EMIm$^+$/BF$_4^-$	1.76			−1.36		
Bi(111)–EMIm$^+$/BF$_4^-$	3.38			−1.79		
C$_{54}$H$_{18}$–EMIm$^+$/BF$_4^-$	1.43			−2.73		
Au(111)–3EMImBF$_4$		−2.75			19.02	
Bi(111)–3EMImBF$_4$		−3.47			11.6	
C$_{54}$H$_{18}$–3EMImBF$_4$		−3.12			12.40	

Then, approximating the ionic dipole as

$$\mu_{ion} = deq \qquad (26)$$

where d is the distance from the surface atom nuclei to the B atom of anion or imidazolium ring of cation, e is elementary electronic charge, and q is the ChelpG ionic charge, we can evaluate each interfacial dipole component contribution (Table 13).

Under certain assumptions, at negative surface charge densities, the magnitude of μ_{ion} is very close to μ_{el} and μ_{solv} values. However, in case of Au(111) and Bi(111) surfaces, this situation changes at positive surface charges, where the magnitude of μ_{solv} is much higher than that at negative surface charges. That results in the considerable role of $\mu_{el} + \mu_{solv}$, which determines the shape of the capacitance (Figure 18) in that surface charge region.

After applying Eq. 15, it becomes possible to calculate the integral capacitance C_{int} values (Figure 18), being very similar for studied surfaces at negative surface charge values, however significantly different at positive potentials. The calculated C_{int} increases with the increase of surface charge density as well as electrode potential above the potential of zero charge.
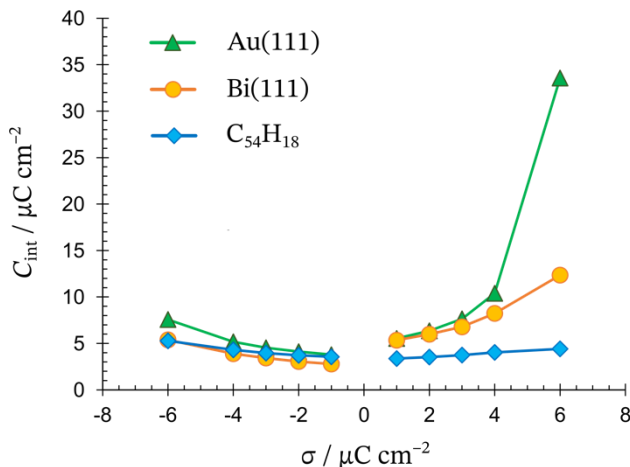

Figure 18. Dependence of the integral capacitance on the surface charge density for interfaces noted in Figure 13.

Table 13. Evaluated dipole moment values (in Debye) for different interfaces at negative and positive surface charge densities.

Surface	$\sigma = -3\ \mu C/cm^2$			$\sigma = +3\ \mu C/cm^2$		
	μ_{ion}	μ_{el}	μ_{solv}	μ_{ion}	μ_{el}	μ_{solv}
Au(111)	22.8	−21.1	18.3	−20.6	19.2	−10.2
Bi(111)	26.4	−23.0	19.5	−28.0	26.2	−14.7
$C_{54}H_{18}$	24.2	−22.7	19.6	−22.7	20.0	−17.6

7.3 Conclusive remarks

We performed analysis of the primary behaviour of $EMImBF_4$ ionic associates adsorbed at Au(111), Bi(111) and $C_{54}H_{18}$ surfaces, focusing on the interfacial geometry and interaction strength between RTIL associate and electrode surfaces under an applied field.

We found that desorption of BF_4^- anion starts at negative surface charge density values for all three of surfaces studied. However, the distance from $EMIm^+$ cation to the surface practically does not change. The presented model shows that the anions and cations interchange upon applying field, *i.e.* charging the surface. On the Au(111) surface the ions are more strongly bond to the surface than on the Bi(111) and $C_{54}H_{18}$ surfaces. The partial charge transfer is more sensitive to the surface charge for Au(111)–$3EMImBF_4$ and $C_{54}H_{18}$–$3EMImBF_4$ models than in case of Bi(111)–$3EMImBF_4$ system.

By analogy with the data of aqueous solution–metal interface study, the interfacial dipole at the interface was split into three different dipole contributions, and each of them was evaluated. The computations show that the anions and cations interchange upon applying an electric field, thus changing the magnitude of the solvent dipole. While at negative surface charge densities the magnitude of ion, surface and solvent dipoles are similar to each other, at positive surface charges, the magnitude of solvent layer dipole decreases. Thus, it plays an essential role in determining the shape of the capacitance *vs.* potential curve.

8. SUMMARY

In this thesis, we investigated the electrical double layer at metal–aqueous solution and metal–ionic liquid interfaces. For both aqueous and ionic liquid interfaces, we focused on the characteristics of interfacial dipole created at metal–electrolyte interface. We analysed its components on the example of the compact layer – the region between the outer Helmholtz plane and the interface.

We started with a computational investigation of interfacial structure and differential capacitance of the electrical double layer at Bi, Ga, and Hg electrodes in aqueous electrolyte solution. The obtained results stress the significant role of the interfacial water layer in the interfacial properties of a metal surface–electrolyte solution interface. Then we gained computational insights into the structure of the metal–ionic liquid interfaces and how it determines the interfacial dipole as well as the differential capacitance. We introduced an ionic bilayer model that accounts for the dipole formed due to the adsorption of counter-ions as well as for the dipole formed due to anion–cation interplay. In a study of an ionic pair at circumcoronene surface, we showed that the covalent bonding significantly reduces the interfacial dipole moment value as well as the potential drop at an electrode–electrolyte interface, thus, leading to the capacitance increase. Comparison of the behaviour of $EMImBF_4$ ionic associates at gold, bismuth and circumcoronene surfaces revealed that electrolyte layer dipole composition and structure play a crucial role in determining the shape of the capacitance *vs.* electrode potential curve.

The conceptual difference between the properties of the aquoues and ionic liquid electrical double layers is dictated by the difference in their molucular and ionic structures. The reported data provide useful information on the water and ionic liquid adsorption on the metal surfaces. The enlighten interaction mechanisms may help to find links between the interfacial structure of the metal–electrolyte interfaces and their performance in energy conversion and storage devices.

9. REFERENCES

[1]   R. Guidelli, W. Schmickler, Electrochimica Acta 45 (2000) 2317–2338.

[2]   M.V. Fedorov, A.A. Kornyshev, Chem. Rev. 114 (2014) 2978–3036.

[3]   D.R. MacFarlane, N. Tachikawa, M. Forsyth, J.M. Pringle, P.C. Howlett, G.D. Elliott, J.H. Davis, M. Watanabe, P. Simon, C.A. Angell, Energy Environ. Sci. 7 (2014) 232–250.

[4]   R. Hayes, G.G. Warr, R. Atkin, Chem. Rev. 115 (2015) 6357–6426.

[5]   A. Lewandowski, M. Galinski, J. Power Sources 173 (2007) 822–828.

[6]   H. Kurig, M. Vestli, K. Tõnurist, A. Jänes, E. Lust, J. Electrochem. Soc. 159 (2012) A944–A951.

[7]   T. Torimoto, T. Tsuda, K. Okazaki, S. Kuwabata, Adv. Mater. 22 (2010) 1196–1221.

[8]   J. Torop, M. Arulepp, T. Sugino, K. Asaka, A. Jänes, E. Lust, A. Aabloo, Langmuir 30 (2014) 2583–2587.

[9]   J. Schaefer, Y. Lu, S. Moganty, P. Agarwal, N. Jayaprakash, L. Archer, Appl. Nanosci. 2 (2012) 91–109.

[10]   B. Li, L. Wang, B. Kang, P. Wang, Y. Qiu, Sol. Energy Mater. Sol. Cells 90 (2006) 549–573.

[11]   R. F De Souza, J. Padilha, R. S Gonc, J. Dupont, Electrochem. Commun. 2 (2003) 728.

[12]   H. Valencia, M. Kohyama, S. Tanaka, H. Matsumoto, Phys. Rev. B 78 (2008) 205402.

[13]   H. Valencia, M. Kohyama, S. Tanaka, H. Matsumoto, J. Chem. Phys. 131 (2009) 244705.

[14]   L. Siinor, K. Lust, E. Lust, ECS Trans. 16 (2009) 559.

[15]   L. Siinor, K. Lust, E. Lust, Electrochem. Commun. 12 (2010) 1058–1061.

[16]   L. Siinor, K. Lust, E. Lust, J. Electrochem. Soc. 157 (2010) F83–F87.

[17]   L. Siinor, C. Siimenson, V. Ivaništšev, K. Lust, E. Lust, J. Electroanal. Chem. 668 (2012) 30–36.

[18]   X. Crispin, V. Geskin, A. Crispin, J. Cornil, R. Lazzaroni, W.R. Salaneck, J.L. Bredas, J Am Chem Soc 124 (2002) 8131–8141.

[19]   S. Trasatti, E. Lust, In: White RE, Conway BE, Bockris JO'M (Eds) Modern Aspects of Electrochemistry, Vol 33, Kluwer/Plenum, New York, 1999.

[20]   J. Carrasco, A. Hodgson, A. Michaelides, Nat. Mater. 11 (2012) 667–674.

[21]   M.A. Henderson, Surf. Sci. Rep. 46 (2002) 1–308.

[22]   A.A. Kornyshev, E. Spohr, M.A. Vorotyntsev, in:, Encycl. Electrochem., Wiley-VCH Verlag GmbH & Co. KGaA, 2007.

[23] E. Lust, in:, A.J. Bard, M. Stratmann, E. Gileadi, M. Urbakh (Eds.), Encycl. Electrochem. Thermodyn. Electrified Interfaces, Wiley VCH, 2002, pp. 188–225.

[24] V. Ivanistsev, R.R. Nazmutdinov, E. Lust, Surf. Sci. 604 (2010) 1919–1927.

[25] V. Ivaništšev, R.R. Nazmutdinov, E. Lust, Surf. Sci. 609 (2013) 91–99.

[26] M. Frisch, G. Truck, H. Schlegel, G. Scuseria, M. Robb, J. Cheeseman, G. Scalmani, V. Barone, B. Mennucci, G. Petersson, others, Inc Wallingford CT (2009).

[27] P.J. Hay, W.R. Wadt, J. Chem. Phys. 82 (1985) 270–283.

[28] C.E. Check, T.O. Faust, J.M. Bailey, B.J. Wright, T.M. Gilbert, L.S. Sunderlin, J. Phys. Chem. A 105 (2001) 8111–8116.

[29] S. Wei, H. Oyanagi, W. Liu, T. Hu, S. Yin, G. Bian, J Non-Cryst Solids 275 (2000) 160–168.

[30] N. Gaston, B. Paulus, K. Rosciszewski, P. Schwerdtfeger, H. Stoll, Phys. Rev. B 74 (2006) 094102.

[31] P. Hofmann, Prog. Surf. Sci. 81 (2006) 191–245.

[32] M. Frisch, others, Inc Wallingford CT (2003).

[33] W. Schmickler, J. Electroanal. Chem. Interfacial Electrochem. 149 (1983) 15–26.

[34] V. Ivaništšev, R.R. Nazmutdinov, E. Lust, Surf. Sci. 604 (2010) 1919–1927.

[35] R.R. Nazmutdinov, M. Probst, K. Heinzinger, J. Electroanal. Chem. 369 (1994) 227–231.

[36] W.R. Fawcett, P.J. Ryan, J. Electroanal. Chem. 649 (2010) 48–52.

[37] E. Spohr, J. Electroanal. Chem. 450 (1998) 327–334.

[38] D.I. Dimitrov, N.D. Raev, K.I. Semerdzhiev, Phys. Chem. Chem. Phys. 3 (2001) 448–452.

[39] S. Trasatti, in:, B.E. Conway, J.O. Bockris (Eds.), Mod. Asp. Electrochem., Springer, 1979, pp. 81–206.

[40] H. Graham, F. Silva, Can. J. Chem. 59 (1981) 1835–1843.

[41] K. Lust, M. Väärtnõu, E. Lust, Electrochimica Acta 45 (2000) 3543–3554.

[42] B.B. Damaskin, A.N. Frumkin, Electrochimica Acta 19 (1974) 173–176.

[43] V.V. Emets, B.B. Damaskin, Russ. J. Electrochem. 45 (2009) 45–57.

[44] J. Forsman, C.E. Woodward, M. Trulsson, J. Phys. Chem. B 115 (2011) 4606–4612.

[45] Y. Lauw, M.D. Horne, T. Rodopoulos, A. Nelson, F.A.M. Leermakers, J. Phys. Chem. B 114 (2010) 11149–11154.

[46] A.A. Kornyshev, J. Phys. Chem. B 111 (2007) 5545–5557.

[47] M.Z. Bazant, B.D. Storey, A.A. Kornyshev, Phys. Rev. Lett. 106 (2011) 046102-4.

[48] D. Henderson, S. Lamperski, J. Chem. Eng. Data 56 (2011) 1204–1208.

[49] M.S. Loth, B. Skinner, B.I. Shklovskii, Phys. Rev. E 82 (2010) 056102-7.

[50] G. Feng, J. Huang, B.G. Sumpter, V. Meunier, R. Qiao, Phys. Chem. Chem. Phys. 13 (2011) 14723–14734.

[51] R.M. Lynden-Bell, A.I. Frolov, M.V. Fedorov, Phys. Chem. Chem. Phys. 14 (2012) 2693–2701.

[52] E. Soolo, D. Brandell, A. Liivat, H. Kasemägi, T. Tamm, A. Aabloo, J. Mol. Model. 18 (2012) 1541–1552.

[53] J. Vatamanu, O. Borodin, D. Bedrov, G.D. Smith, J. Phys. Chem. C 116 (2012) 7940–7951.

[54] K. Kirchner, T. Kirchner, V. Ivaništšev, M.V. Fedorov, Electrochimica Acta 110 (2013) 762–771.

[55] C. Merlet, D.T. Limmer, M. Salanne, R. van Roij, P.A. Madden, D. Chandler, B. Rotenberg, J. Phys. Chem. C (2014).

[56] V. Ivaništšev, S. O'Connor, M.V. Fedorov, Electrochem. Commun. 48 (2014) 61–64.

[57] T. Pajkossy, D.M. Kolb, Electrochem. Commun. 13 (2011) 284–286.

[58] V. Lockett, M. Horne, R. Sedev, T. Rodopoulos, J. Ralston, Phys. Chem. Chem. Phys. 12 (2010) 12499–12512.

[59] M. Drüschler, B. Huber, B. Roling, J. Phys. Chem. C 115 (2011) 6802–6808.

[60] B. Roling, M. Drüschler, B. Huber, Faraday Discuss. 154 (2011) 303–311.

[61] S. Baldelli, Acc. Chem. Res. 41 (2008) 421–431.

[62] S. Baldelli, J. Phys. Chem. Lett. 4 (2013) 244–252.

[63] R. Costa, C.M. Pereira, F. Silva, Phys. Chem. Chem. Phys. 12 (2010) 11125–11132.

[64] M.M. Islam, M.T. Alam, T. Ohsaka, J. Phys. Chem. C 112 (2008) 16568–16574.

[65] V. Ivaništšev, A. Ruzanov, K. Lust, E. Lust, J. Electrochem. Soc. 160 (2013) H368–H375.

[66] L. Siinor, R. Arendi, K. Lust, E. Lust, J. Electroanal. Chem. 689 (2013) 51–56.

[67] M.T. Alam, J. Masud, M.M. Islam, T. Okajima, T. Ohsaka, J. Phys. Chem. C 115 (2011) 19797–19804.

[68] C. Gomes, R. Costa, C.M. Pereira, A.F. Silva, RSC Adv. 4 (2014) 28914–28921.

[69] Y. Liu, Y.-X. Yuan, X.-R. Wang, N. Zhang, M.-M. Xu, J.-L. Yao, R.-A. Gu, J. Electroanal. Chem. 728 (2014) 10–17.

[70] O. Oll, T. Romann, P. Pikma, E. Lust, J. Electroanal. Chem. 778 (2016) 41–48.

[71] Y. Su, J. Yan, M. Li, M. Zhang, B. Mao, J. Phys. Chem. C 117 (2013) 205–212.

[72] M.V. Fedorov, A.A. Kornyshev, Electrochimica Acta 53 (2008) 6835–6740.

[73] N. Georgi, A.A. Kornyshev, M.V. Fedorov, J. Electroanal. Chem. 649 (2010) 261–267.

[74] J. Vatamanu, O. Borodin, G.D. Smith, J. Phys. Chem. B 115 (2011) 3073–3084.

[75] R. Atkin, N. Borisenko, M. Drüschler, F. Endres, R. Hayes, B. Huber, B. Roling, J. Mol. Liq. 192 (2014) 44–54.

[76] E. Sloutskin, B.M. Ocko, L. Tamam, I. Kuzmenko, T. Gog, M. Deutsch, J. Am. Chem. Soc. 127 (2005) 7796–7804.

[77] M. Mezger, H. Schröder, H. Reichert, S. Schramm, J.S. Okasinski, S. Schöder, V. Honkimäki, M. Deutsch, B.M. Ocko, J. Ralston, M. Rohwerder, M. Stratmann, H. Dosch, Science 322 (2008) 424–428.

[78] N. Nishi, Y. Yasui, T. Uruga, H. Tanida, T. Yamada, S. Nakayama, H. Matsuoka, T. Kakiuchi, J. Chem. Phys. 132 (2010) 164705–6.

[79] N. Nanbu, Y. Sasaki, F. Kitamura, Electrochem. Commun. 5 (2003) 383–387.

[80] T. Romann, O. Oll, P. Pikma, E. Lust, Electrochem. Commun. 23 (2012) 118–121.

[81] T. Romann, O. Oll, P. Pikma, H. Tamme, E. Lust, Electrochimica Acta 125 (2014) 183–190.

[82] S.S. Moganty, R.E. Baltus, D. Roy, Chem. Phys. Lett. 483 (2009) 90–94.

[83] A. Foelske-Schmitz, D. Weingarth, R. Kötz, Electrochimica Acta 56 (2011) 10321–10331.

[84] M. Gnahm, C. Müller, R. Répánszki, T. Pajkossy, D.M. Kolb, Phys. Chem. Chem. Phys. 13 (2011) 11627–11633.

[85] M. Gnahm, T. Pajkossy, D.M. Kolb, Electrochimica Acta 55 (2010) 6212–6217.

[86] Y.Z. Su, Y.C. Fu, J.W. Yan, Z.B. Chen, B.W. Mao, Angew. Chem.-Int. Ed. 48 (2009) 5148–5151.

[87] G.-B. Pan, W. Freyland, Chem. Phys. Lett. 427 (2006) 96–100.

[88] A.A. Kornyshev, R. Qiao, J. Phys. Chem. C 118 (2014) 18285–18290.

[89] V. Ivaništšev, M.V. Fedorov, Electrochem. Soc. Interface 23 (2014) 65–69.

[90] L. Martínez, R. Andrade, E.G. Birgin, J.M. Martínez, J. Comput. Chem. 30 (2009) 2157–2164.

[91] S.R. Bahn, K.W. Jacobsen, Comput. Sci. Eng. 4 (2002) 56–66.

[92] A. Ruzanov, M. Lembinen, P. Jakovits, S.N. Srirama, I.V. Voroshylova, M.N.D.S. Cordeiro, C.M. Pereira, J. Rossmeisl, V.B. Ivaništšev, Phys. Chem. Chem. Phys. 20 (2018) 10275–10285.

[93] J. Enkovaara, C. Rostgaard, J.J. Mortensen, J. Chen, M. Dułak, L. Ferrighi, J. Gavnholt, C. Glinsvad, V. Haikola, H.A. Hansen, H.H. Kristoffersen, M. Kuisma, A.H. Larsen, L. Lehtovaara, M. Ljungberg, O. Lopez-Acevedo, P.G. Moses, J. Ojanen, T. Olsen, V. Petzold, N.A. Romero, J. Stausholm-Møller, M. Strange, G.A. Tritsaris, M. Vanin, M. Walter, B. Hammer, H. Häkkinen, G.K.H. Madsen, R.M. Nieminen, J.K. Nørskov, M. Puska, T.T. Rantala, J. Schiøtz, K.S. Thygesen, K.W. Jacobsen, J. Phys. Condens. Matter 22 (2010) 253202.

[94] B. Hammer, L.B. Hansen, J.K. Nørskov, Phys. Rev. B 59 (1999) 7413–7421.

[95] S. Tsuzuki, H. Tokuda, K. Hayamizu, M. Watanabe, J. Phys. Chem. B 109 (2005) 16474–16481.

[96] A.R. Choudhury, N. Winterton, A. Steiner, A.I. Cooper, K.A. Johnson, J. Am. Chem. Soc. 127 (2005) 16792–16793.

[97] K. Matsumoto, R. Hagiwara, Z. Mazej, P. Benkic, B. Zemva, Solid State Sci. 8 (2006) 1250–1257.

[98] I. Lage-Estebanez, A. Ruzanov, J.M.G. de la Vega, M.V. Fedorov, V.B. Ivaništšev, Phys. Chem. Chem. Phys. 18 (2016) 2175–2182.

[99] A. Deyko, K.R.J. Lovelock, J.-A. Corfield, A.W. Taylor, P.N. Gooden, I.J. Villar-Garcia, P. Licence, R.G. Jones, V.G. Krasovskiy, E.A. Chernikova, L.M. Kustov, Phys. Chem. Chem. Phys. 11 (2009) 8544.

[100] D.H. Zaitsau, K. Fumino, V.N. Emel'yanenko, A.V. Yermalayeu, R. Ludwig, S.P. Verevkin, ChemPhysChem 13 (2012) 1868–1876.

[101] J.-P. Schermann, Spectroscopy and Modeling of Biomolecular Building Blocks, Elsevier, 2007.

[102] G.L. Gutsev, P. Jena, R.J. Bartlett, Chem. Phys. Lett. 292 (1998) 289–294.

[103] E.I. Izgorodina, U.L. Bernard, P.M. Dean, J.M. Pringle, D.R. MacFarlane, Cryst. Growth Des. 9 (2009) 4834–4839.

[104] J. Rossmeisl, E. Skúlason, M.E. Björketun, V. Tripković, J.K. Nørskov, Chem. Phys. Lett. 466 (2008) 68–71.

[105] E. Skúlason, V. Tripkovic, M.E. Björketun, S. Gudmundsdóttir, G. Karlberg, J. Rossmeisl, T. Bligaard, H. Jónsson, J.K. Nørskov, J. Phys. Chem. C 114 (2010) 18182–18197.

[106] M. Nielsen, M.E. Björketun, M.H. Hansen, J. Rossmeisl, Surf. Sci. 631 (2015) 2–7.

[107] G.V. Hansson, S.A. Flodström, Phys. Rev. B 18 (1978) 1572–1585.

[108] T.A. Manz, N.G. Limas, RSC Adv. 6 (2016) 47771–47801.

[109] N.G. Limas, T.A. Manz, RSC Adv. 6 (2016) 45727–45747.

[110] M. Mizoshiri, T. Nagao, Y. Mizoguchi, M. Yao, J. Chem. Phys. 132 (2010) 164510.

[111] O. Oll, T. Romann, C. Siimenson, E. Lust, Electrochem. Commun. 82 (2017) 39–42.

[112] A. Yochelis, Phys. Chem. Chem. Phys. 16 (2014) 2836–2841.

[113] V. Ivaništšev, K. Kirchner, T. Kirchner, M.V. Fedorov, J. Phys. Condens. Matter 27 (2015) 102101.

[114] Z. Hu, J. Vatamanu, O. Borodin, D. Bedrov, Phys. Chem. Chem. Phys. 15 (2013) 14234–14247.

[115] R. Capozza, A. Vanossi, A. Benassi, E. Tosatti, J. Chem. Phys. 142 (2015) 064707.

[116] V.B. Ivaništšev, K. Kirchner, M.V. Fedorov, Https://Arxiv.Org/Abs/1711.06854 (2017).

[117] Z.E. Hughes, T.R. Walsh, Nanoscale 7 (2015) 6883–6908.

[118] M.V. Fedorov, A.A. Kornyshev, Chem. Rev. 114 (2014) 2978–3036.

[119] D.R. MacFarlane, N. Tachikawa, M. Forsyth, J.M. Pringle, P.C. Howlett, G.D. Elliott, J.H. Davis, M. Watanabe, P. Simon, C.A. Angell, Energy Environ. Sci. 7 (2014) 232–250.

[120] D. Wagle, G. Kamath, G.A. Baker, J. Phys. Chem. C 117 (2013) 4521–4532.

[121] B. Sütay, M. Yurtsever, E. Yurtsever, J. Mol. Model. 20 (2014) 1–10.

[122] T.A. Baker, M. Head-Gordon, J. Phys. Chem. A 114 (2010) 10326–10333.

[123] A.J. Cohen, P. Mori-Sánchez, W. Yang, Science 321 (2008) 792–794.

[124] S. Grimme, W. Hujo, B. Kirchner, Phys. Chem. Chem. Phys. 14 (2012) 4875–4883.

[125] H. Weber, T. Bredow, B. Kirchner, J. Phys. Chem. C 119 (2015) 15137–15149.

[126] I. Lage-Estebanez, L. del Olmo, R. López, J.M. García de la Vega, J. Comput. Chem. 38 (2017) 530–540.

[127] S. Patchkovskii, T. Ziegler, J. Chem. Phys. 116 (2002) 7806–7813.

[128] S. Patchkovskii, T. Ziegler, J. Phys. Chem. A 106 (2002) 1088–1099.

[129] S. Patchkovskii, J. Autschbach, T. Ziegler, J. Chem. Phys. 115 (2001) 26–42.

[130] S. Leach, in:, Interstellar Dust, Springer, Dordrecht, 1989, pp. 155–171.

[131] X.-L. Fan, X.-Q. Wang, J.-T. Wang, H.-D. Li, Phys. Lett. A 378 (2014) 1379–1382.

[132] M. Winter, J.O. Besenhard, M.E. Spahr, P. Novák, Adv. Mater. 10 (1998) 725–763.

[133] R. Mitsuhashi, Y. Suzuki, Y. Yamanari, H. Mitamura, T. Kambe, N. Ikeda, H. Okamoto, A. Fujiwara, M. Yamaji, N. Kawasaki, Y. Maniwa, Y. Kubozono, Nature 464 (2010) 76–79.

[134] M.-C. Lin, M. Gong, B. Lu, Y. Wu, D.-Y. Wang, M. Guan, M. Angell, C. Chen, J. Yang, B.-J. Hwang, H. Dai, Nature advance online publication (2015).

[135] M. Armand, F. Endres, D.R. MacFarlane, H. Ohno, B. Scrosati, Nat. Mater. 8 (2009) 621–629.

[136] T. Tooming, T. Thomberg, H. Kurig, A. Jänes, E. Lust, J. Power Sources 280 (2015) 667–677.

[137] T. Romann, E. Anderson, P. Pikma, H. Tamme, P. Möller, E. Lust, Electrochem. Commun. 74 (2017) 38–41.

[138] A. Jänes, J. Eskusson, T. Thomberg, T. Romann, E. Lust, J. Energy Chem. (n.d.).

[139] C. Siimenson, L. Siinor, K. Lust, E. Lust, J. Electroanal. Chem. 730 (2014) 59–64.

[140] C. Siimenson, L. Siinor, K. Lust, E. Lust, ECS Electrochem. Lett. 4 (2015) H62–H65.

[141] C. Siimenson, M. Lembinen, O. Oll, L. Läll, M. Tarkanovskaja, V. Ivaništšev, L. Siinor, T. Thomberg, K. Lust, E. Lust, J. Electrochem. Soc. 163 (2016) H723–H730.

[142] L. Siinor, J. Poom, C. Siimenson, K. Lust, E. Lust, J. Electroanal. Chem. 719 (2014) 133–137.

[143] J. Eskusson, A. Jänes, A. Kikas, L. Matisen, E. Lust, J. Power Sources 196 (2011) 4109–4116.

[144] M. Salanne, Top. Curr. Chem. Cham 375 (2017) 63.

[145] V. Gómez-González, B. Docampo-Álvarez, T. Méndez-Morales, O. Cabeza, V. B. Ivaništšev, M. V. Fedorov, L. J. Gallego, L. M. Varela, Phys. Chem. Chem. Phys. 19 (2017) 846–853.

[146] M.D. Hanwell, D.E. Curtis, D.C. Lonie, T. Vandermeersch, E. Zurek, G.R. Hutchison, J. Cheminformatics 4 (2012) 17.

[147] F. Neese, Wiley Interdiscip. Rev. Comput. Mol. Sci. 2 (2012) 73–78.

[148] J.P. Perdew, K. Burke, M. Ernzerhof, Phys. Rev. Lett. 77 (1996) 3865–3868.

[149] S. Grimme, J.G. Brandenburg, C. Bannwarth, A. Hansen, J. Chem. Phys. 143 (2015) 054107.

[150] S. Grimme, Wiley Interdiscip. Rev. Comput. Mol. Sci. 1 (2011) 211–228.

[151] S. Grimme, J. Antony, S. Ehrlich, H. Krieg, J. Chem. Phys. 132 (2010) 154104.

[152] H. Kruse, S. Grimme, J. Chem. Phys. 136 (2012) 154101.

[153] A. Ruzanov, M. Lembinen, H. Ers, J.M. García de la Vega, I. Lage-Estebanez, E. Lust, V.B. Ivaništšev, J. Phys. Chem. C 122 (2018) 2624–2631.

[154] C.M. Breneman, K.B. Wiberg, J. Comput. Chem. 11 (1990) 361–373.

[155] J. Lemus, C.M.S.S. Neves, C.F.C. Marques, M.G. Freire, J.A.P. Coutinho, J. Palomar, Environ. Sci. Process. Impacts 15 (2013) 1752–1759.

[156] J. Lemus, J. Palomar, M.A. Gilarranz, J.J. Rodriguez, Ind. Eng. Chem. Res. 52 (2013) 2969–2976.

[157] S. Hassan, T. Yasin, Int. J. Environ. Sci. Technol. 12 (2015) 2711–2722.

[158] L. Siinor, C. Siimenson, K. Lust, E. Lust, Electrochem. Commun. 35 (2013) 5–7.

[159] O. Oll, C. Siimenson, K. Lust, G. Gorbatovski, E. Lust, Electrochimica Acta 247 (2017) 910–919.

[160] R.N. Kuklin, V.V. Emets, Russ. J. Phys. Chem. B 3 (2009) 818–825.

[161] L. Guo, Y. Ou, X. Shen, S. Kaya, W. Shei, R. Zhang, X. Zheng, J. Wang, Int. J. Electrochem. Sci. 12 (2017).

[162] K. Lust, E. Lust, J. Electroanal. Chem. 552 (2003) 129–139.

[163] C.F. Guerra, J.G. Snijders, G. te Velde, E.J. Baerends, Theor. Chem. Acc. 99 (1998) 391–403.

[164] J.S. Wilkes, M.J. Zaworotko, Chem. Commun. 13 (1992) 965–967.

[165] S.F.L. Mertens, C. Vollmer, A. Held, M.H. Aguirre, M. Walter, C. Janiak, T. Wandlowski, Angew. Chem. Int. Ed. 50 (2011) 9735–9738.

[166] R.S. Mulliken, J. Chem. Phys. 23 (1955) 1833–1840.

[167] A.E. Reed, L.A. Curtiss, F. Weinhold, Chem. Rev. 88 (1988) 899–926.

[168] A.E. Reed, R.B. Weinstock, F. Weinhold, J. Chem. Phys. 83 (1985) 735–746.

[169] J.D. Thompson, J.D. Xidos, T.M. Sonbuchner, C.J. Cramer, D.G. Truhlar, PhysChemComm 5 (2002) 117–134.

10. SUMMARY IN ESTONIAN

Metalli–vesilahuse ja metalli–ioonse vedeliku elektrilise kakskkihi arvutuslik uurimine

Käesolevas teadustöös uurisime metalli ja vesilahuse ning metalli ja ioonse vedeliku vahelist elektrilist kaksikkihti, keskendudes pindkihi dipoolse struktuuri analüüsile. Hindasime selle komponente elektrilise kaksikkihi kompaktses osas, mis jääb Helmholtzi välise kihi ja metalli pindkihi vahele.

Alustasime pindkihi struktuuri ning elektrilise kaksikkihi diferentsiaal-mahtuvuse arvutusliku uuringuga vismuti, galliumi ja elavhõbeda pinnal vesilahustes. Saadud tulemused kinnitavad molekulide adsorptsiooni olulist rolli elektrilise kaksikkihi omaduste kujunemisel. Seejärel kogusime arvutuslikke andmeid metalli ja ioonse vedeliku pindkihi struktuuri kohta, ning uurisime kuidas see määrab pindkihi dipoolse ehituse ning diferentsiaal-mahtuvuse. Kasutasime ioonse kaksikkihi mudelit, mis sobib nii vastas-ioonide adsorptsiooni tõttu tekkinud dipooli kui ka anioonide ja katioonide vastastikuste mõjutuste tõttu tekkinud dipooli kirjeldamiseks. Süsiniku pinnal paiknevat ioonpaari käsitlevas uuringus näitasime, et kovalentne side vähendab oluliselt dipoolmomendi väärtust ning potentsiaalilangust elektroodi–elektrolüüdi pindkihis, mille tulemusena suureneb elektrimahtuvus. $EMImBF_4$ ioonassotsiaatide võrdlemisel kulla, vismuti ja süsiniku pinnal selgus, et elektrolüüdikihi dipool mõjutab oluliselt mahtuvuse elektroodi potentsiaalist sõltuvuse kõvera kuju.

Põhimõtteline erinevus vesilahuse ja ioonse vedeliku elektrilise kaksik-kihi omaduste vahel tuleneb nende molekulaarse ja ioonse struktuuri erine-vusest. Esitatud andmed annavad kasulikku teavet vesilahuse ja ioonvede-liku adsorptsiooni kohta erinevatel metallidel. Teave nende tegurite vastas-tikuste mõjude kohta võib aidata leida seoseid metalli ja elektrolüüdi pind-kihi struktuuri ning pindkihtide toimimise vahel energia muundamise ja salvestamise seadmetes.

11. ACKNOWLEDGEMENTS

First of all, I would like to express my greatest gratitude to my supervisors Ph.D. Vladislav Ivaništšev and Prof. Enn Lust for their invaluable comments, scientific guidance and support during all these time of my studies in the University of Tartu.

I am very thankful to Prof. Renat R. Nazmutdinov for his continuous support throughout my study and for all the advice and great ideas he has been sharing with me. I would like to thank all my colleagues from the University of Tartu for the helpful discussions and warm atmosphere: Meeri Lembinen, Heigo Ers, Karl Karu, Ove Oll and Maksim Mishin, and also Isabel Lage-Estebanez from Autonomous University of Madrid and Iiulia Voroshilova from University of Porto.

I am extremely grateful for my family and friends who have always believed in me even in most difficult moments and motivated me strongly to finish my chosen path.

12. PUBLICATIONS

CURRICULUM VITAE

Name: Anton Ruzanov
Date of birth: July 14, 1987
Citizenship: Estonian
Marital status: Married
Contact: Vana-Kuuli 5–68, 13619 Tallinn, Estonia
E-mail: anton.ruzanov@ut.ee

Education:

2013–...	University of Tartu – Chemistry *Ph.D.* student
2010–2012	University of Tartu – Master's degree in Chemistry
2006–2010	University of Tartu – Batchelor's degree in Materials Science
2003–2006	Juhkentali Gymnasium (secondary education)
1994–2003	Juhkentali School (basic education)

Professional employment:

2018–...	Aston Synthetics, Quality control engineer
2014–2018	ANF Technology, Head of testing laboratory
2011–2014	Molycorp Silmet, Chemical engineer
2009–2012	University of Tartu, Institute of Chemistry, Chemist

List of publications:

1. **A. Ruzanov**, M. Lembinen, I.V. Voroshylova, P. Jakovits, S.N. Srirama, M. Natalia D.S Cordeiro, C.M. Pereira, J. Rossmeisl, V. Ivaništšev, On the thickness of the double layer in ionic liquids, Physical Chemistry Chemical Physics Journal, 20 (2018) 10275–10285.

2. **A. Ruzanov**, M. Lembinen, H. Ers, J.M. Garsía de la Vega, I. Lage-Estebanez, E. Lust, V. Ivaništšev, DFT Study of Ionic Liquids Adsorption on Circumcoronene Shaped Graphene, Journal of Physical Chemistry, 122 (2018) 2624–2631.

3. **A. Ruzanov**, K. Karu, V. Ivaništšev, R.R. Nazmutdinov, E. Lust, Interplay between the hydrophilicity of metal electrodes and their interfacial capacitance, Electrochimica Acta, 210 (2016) 615–621.

4. I. Lage-Estebanez, **A. Ruzanov**, J. M. Garsía de la Vega, M.V. Fedorov, V. Ivaništšev, Self-interaction error in DFT-based modelling of ionic liquids, Physical Chemistry Chemical Physics, 18 (2016) 2175–2182.

5. K. Karu, **A. Ruzanov**, H. Ers, V. Ivaništšev, I. Lage-Estebanez, J.M. Garsía de la Vega, Predictions of physicochemical properties of ionic liquids with DFT, Computation, 4 (2016) 25.

6. E. Lust, L. Siinor, H. Kurig, T. Romann, V. Ivaništšev, C. Siimenson, T. Thomberg, J. Kruusma, K. Lust, P. Pikma, E. Anderson, V. Grozovski, R. Palm, L. Läll, **A. Ruzanov**, T. Tooming, O. Oll, A. Jänes, Characteristics of capacitors based on ionic liquids: from dielectric polymers to redox-active adsorbed species, ECS Transactions, 75 (2016) 161–170.

7. V. Ivaništšev, **A. Ruzanov**, K. Lust, E. Lust, Comparative impedance study of Cd(0001) electrode in EMImBF$_4$ and KI aqueous solution at different temperatures, Journal of the Electrochemical Society, 160 (2013) H368–H375.

Participation in international conferences:

1. **A. Ruzanov**, K. Karu, I. Lage-Estebanez, V. Ivaništšev, E. Lust, J.M. Garsía de la Vega, DFT-based modelling of associates of ionic liquid ions, 6th Baltic Electrochemistry Conference, Helsinki, Finland, 15–17 June 2016.

ELULOOKIRJELDUS

Nimi: Anton Ruzanov
Sünniaeg: 14. Juuli 1987
Kodakondsus: Eestlane
Perekonnaseis: Abielus
Kontakt: Vana-Kuuli 5–68, 13619 Tallinn, Estonia
E-mail: anton.ruzanov@ut.ee

Haridus:

2013–... Tartu Ülikool – keemia doktorant
2010–2012 Tartu Ülikool – magistrikraad keemias
2006–2010 Tartu Ülikool – bakalaureusekraad materjaliteaduses
2003–2006 Juhkentali Gümnaasium (keskharidus)
1994–2003 Juhkentali Kool (põhiharidus)

Töökogemus:

2018–... Aston Synthetics, kvaliteediinsener
2014–2018 ANF Technology, katselabori juht
2011–2014 Molycorp Silmet, keemia insener
2009–2012 Tartu Ülikooli keemia instituut, keemik

Teaduspublikatsioonid:

1. **A. Ruzanov**, M. Lembinen, I.V. Voroshylova, P. Jakovits, S.N. Srirama, M. Natalia D.S Cordeiro, C.M. Pereira, J. Rossmeisl, V. Ivaništšev, On the thickness of the double layer in ionic liquids, Physical Chemistry Chemical Physics Journal, 20 (2018) 10275–10285.

2. **A. Ruzanov**, M. Lembinen, H. Ers, J.M. Garsía de la Vega, I. Lage-Estebanez, E. Lust, V. Ivaništšev, DFT Study of Ionic Liquids Adsorption on Circumcoronene Shaped Graphene, Journal of Physical Chemistry, 122 (2018) 2624–2631.

3. **A. Ruzanov**, K. Karu, V. Ivaništšev, R.R. Nazmutdinov, E. Lust, Interplay between the hydrophilicity of metal electrodes and their interfacial capacitance, Electrochimica Acta, 210 (2016) 615–621.

4. I. Lage-Estebanez, **A. Ruzanov**, J. M. Garsía de la Vega, M.V. Fedorov, V. Ivaništšev, Self-interaction error in DFT-based modelling of ionic liquids, Physical Chemistry Chemical Physics, 18 (2016) 2175–2182.

5. K. Karu, **A. Ruzanov**, H. Ers, V. Ivaništšev, I. Lage-Estebanez, J.M. Garsía de la Vega, Predictions of physicochemical properties of ionic liquids with DFT, Computation, 4 (2016) 25.

6. E. Lust, L. Siinor, H. Kurig, T. Romann, V. Ivaništšev, C. Siimenson, T. Thomberg, J. Kruusma, K. Lust, P. Pikma, E. Anderson, V. Grozovski, R. Palm, L. Läll, **A. Ruzanov**, T. Tooming, O. Oll, A. Jänes, Characteristics of capacitors based on ionic liquids: from dielectric polymers to redox-active adsorbed species, ECS Transactions, 75 (2016) 161–170.

7. V. Ivaništšev, **A. Ruzanov**, K. Lust, E. Lust, Comparative impedance study of Cd(0001) electrode in $EMImBF_4$ and KI aqueous solution at different temperatures, Journal of the Electrochemical Society, 160 (2013) H368–H375.

Rahvusvahelistel konverentsidel osalemine:

1. **A. Ruzanov**, K. Karu, I. Lage-Estebanez, V. Ivaništšev, E. Lust, J.M. Garsía de la Vega, DFT-based modelling of associates of ionic liquid ions, 6th Baltic Electrochemistry Conference, Helsinki, Soome, 15–17 Juuni 2016.

DISSERTATIONES CHIMICAE
UNIVERSITATIS TARTUENSIS

1. **Toomas Tamm.** Quantum-chemical simulation of solvent effects. Tartu, 1993, 110 p.
2. **Peeter Burk.** Theoretical study of gas-phase acid-base equilibria. Tartu, 1994, 96 p.
3. **Victor Lobanov.** Quantitative structure-property relationships in large descriptor spaces. Tartu, 1995, 135 p.
4. **Vahur Mäemets.** The ^{17}O and ^{1}H nuclear magnetic resonance study of H_2O in individual solvents and its charged clusters in aqueous solutions of electrolytes. Tartu, 1997, 140 p.
5. **Andrus Metsala.** Microcanonical rate constant in nonequilibrium distribution of vibrational energy and in restricted intramolecular vibrational energy redistribution on the basis of slater's theory of unimolecular reactions. Tartu, 1997, 150 p.
6. **Uko Maran.** Quantum-mechanical study of potential energy surfaces in different environments. Tartu, 1997, 137 p.
7. **Alar Jänes.** Adsorption of organic compounds on antimony, bismuth and cadmium electrodes. Tartu, 1998, 219 p.
8. **Kaido Tammeveski.** Oxygen electroreduction on thin platinum films and the electrochemical detection of superoxide anion. Tartu, 1998, 139 p.
9. **Ivo Leito.** Studies of Brønsted acid-base equilibria in water and non-aqueous media. Tartu, 1998, 101 p.
10. **Jaan Leis.** Conformational dynamics and equilibria in amides. Tartu, 1998, 131 p.
11. **Toonika Rinken.** The modelling of amperometric biosensors based on oxidoreductases. Tartu, 2000, 108 p.
12. **Dmitri Panov.** Partially solvated Grignard reagents. Tartu, 2000, 64 p.
13. **Kaja Orupõld.** Treatment and analysis of phenolic wastewater with microorganisms. Tartu, 2000, 123 p.
14. **Jüri Ivask.** Ion Chromatographic determination of major anions and cations in polar ice core. Tartu, 2000, 85 p.
15. **Lauri Vares.** Stereoselective Synthesis of Tetrahydrofuran and Tetrahydropyran Derivatives by Use of Asymmetric Horner-Wadsworth-Emmons and Ring Closure Reactions. Tartu, 2000, 184 p.
16. **Martin Lepiku.** Kinetic aspects of dopamine D_2 receptor interactions with specific ligands. Tartu, 2000, 81 p.
17. **Katrin Sak.** Some aspects of ligand specificity of P2Y receptors. Tartu, 2000, 106 p.
18. **Vello Pällin.** The role of solvation in the formation of iotsitch complexes. Tartu, 2001, 95 p.
19. **Katrin Kollist.** Interactions between polycyclic aromatic compounds and humic substances. Tartu, 2001, 93 p.

20. **Ivar Koppel.** Quantum chemical study of acidity of strong and superstrong Brønsted acids. Tartu, 2001, 104 p.
21. **Viljar Pihl.** The study of the substituent and solvent effects on the acidity of OH and CH acids. Tartu, 2001, 132 p.
22. **Natalia Palm.** Specification of the minimum, sufficient and significant set of descriptors for general description of solvent effects. Tartu, 2001, 134 p.
23. **Sulev Sild.** QSPR/QSAR approaches for complex molecular systems. Tartu, 2001, 134 p.
24. **Ruslan Petrukhin.** Industrial applications of the quantitative structure-property relationships. Tartu, 2001, 162 p.
25. **Boris V. Rogovoy.** Synthesis of (benzotriazolyl)carboximidamides and their application in relations with *N*- and *S*-nucleophyles. Tartu, 2002, 84 p.
26. **Koit Herodes.** Solvent effects on UV-vis absorption spectra of some solvatochromic substances in binary solvent mixtures: the preferential solvation model. Tartu, 2002, 102 p.
27. **Anti Perkson.** Synthesis and characterisation of nanostructured carbon. Tartu, 2002, 152 p.
28. **Ivari Kaljurand.** Self-consistent acidity scales of neutral and cationic Brønsted acids in acetonitrile and tetrahydrofuran. Tartu, 2003, 108 p.
29. **Karmen Lust.** Adsorption of anions on bismuth single crystal electrodes. Tartu, 2003, 128 p.
30. **Mare Piirsalu.** Substituent, temperature and solvent effects on the alkaline hydrolysis of substituted phenyl and alkyl esters of benzoic acid. Tartu, 2003, 156 p.
31. **Meeri Sassian.** Reactions of partially solvated Grignard reagents. Tartu, 2003, 78 p.
32. **Tarmo Tamm.** Quantum chemical modelling of polypyrrole. Tartu, 2003. 100 p.
33. **Erik Teinemaa.** The environmental fate of the particulate matter and organic pollutants from an oil shale power plant. Tartu, 2003. 102 p.
34. **Jaana Tammiku-Taul.** Quantum chemical study of the properties of Grignard reagents. Tartu, 2003. 120 p.
35. **Andre Lomaka.** Biomedical applications of predictive computational chemistry. Tartu, 2003. 132 p.
36. **Kostyantyn Kirichenko.** Benzotriazole – Mediated Carbon–Carbon Bond Formation. Tartu, 2003. 132 p.
37. **Gunnar Nurk.** Adsorption kinetics of some organic compounds on bismuth single crystal electrodes. Tartu, 2003, 170 p.
38. **Mati Arulepp.** Electrochemical characteristics of porous carbon materials and electrical double layer capacitors. Tartu, 2003, 196 p.
39. **Dan Cornel Fara.** QSPR modeling of complexation and distribution of organic compounds. Tartu, 2004, 126 p.
40. **Riina Mahlapuu.** Signalling of galanin and amyloid precursor protein through adenylate cyclase. Tartu, 2004, 124 p.

41. **Mihkel Kerikmäe.** Some luminescent materials for dosimetric applications and physical research. Tartu, 2004, 143 p.
42. **Jaanus Kruusma.** Determination of some important trace metal ions in human blood. Tartu, 2004, 115 p.
43. **Urmas Johanson.** Investigations of the electrochemical properties of poly-pyrrole modified electrodes. Tartu, 2004, 91 p.
44. **Kaido Sillar.** Computational study of the acid sites in zeolite ZSM-5. Tartu, 2004, 80 p.
45. **Aldo Oras.** Kinetic aspects of dATPαS interaction with P2Y$_1$ receptor. Tartu, 2004, 75 p.
46. **Erik Mölder.** Measurement of the oxygen mass transfer through the air-water interface. Tartu, 2005, 73 p.
47. **Thomas Thomberg.** The kinetics of electroreduction of peroxodisulfate anion on cadmium (0001) single crystal electrode. Tartu, 2005, 95 p.
48. **Olavi Loog.** Aspects of condensations of carbonyl compounds and their imine analogues. Tartu, 2005, 83 p.
49. **Siim Salmar.** Effect of ultrasound on ester hydrolysis in aqueous ethanol. Tartu, 2006, 73 p.
50. **Ain Uustare.** Modulation of signal transduction of heptahelical receptors by other receptors and G proteins. Tartu, 2006, 121 p.
51. **Sergei Yurchenko.** Determination of some carcinogenic contaminants in food. Tartu, 2006, 143 p.
52. **Kaido Tämm.** QSPR modeling of some properties of organic compounds. Tartu, 2006, 67 p.
53. **Olga Tšubrik.** New methods in the synthesis of multisubstituted hydra-zines. Tartu. 2006, 183 p.
54. **Lilli Sooväli.** Spectrophotometric measurements and their uncertainty in chemical analysis and dissociation constant measurements. Tartu, 2006, 125 p.
55. **Eve Koort.** Uncertainty estimation of potentiometrically measured ph and pK_a values. Tartu, 2006, 139 p.
56. **Sergei Kopanchuk.** Regulation of ligand binding to melanocortin receptor subtypes. Tartu, 2006, 119 p.
57. **Silvar Kallip.** Surface structure of some bismuth and antimony single crystal electrodes. Tartu, 2006, 107 p.
58. **Kristjan Saal.** Surface silanization and its application in biomolecule coupling. Tartu, 2006, 77 p.
59. **Tanel Tätte.** High viscosity Sn(OBu)$_4$ oligomeric concentrates and their applications in technology. Tartu, 2006, 91 p.
60. **Dimitar Atanasov Dobchev**. Robust QSAR methods for the prediction of properties from molecular structure. Tartu, 2006, 118 p.
61. **Hannes Hagu**. Impact of ultrasound on hydrophobic interactions in solutions. Tartu, 2007, 81 p.
62. **Rutha Jäger.** Electroreduction of peroxodisulfate anion on bismuth electrodes. Tartu, 2007, 142 p.

63. **Kaido Viht.** Immobilizable bisubstrate-analogue inhibitors of basophilic protein kinases: development and application in biosensors. Tartu, 2007, 88 p.

64. **Eva-Ingrid Rõõm.** Acid-base equilibria in nonpolar media. Tartu, 2007, 156 p.

65. **Sven Tamp.** DFT study of the cesium cation containing complexes relevant to the cesium cation binding by the humic acids. Tartu, 2007, 102 p.

66. **Jaak Nerut.** Electroreduction of hexacyanoferrate(III) anion on Cadmium (0001) single crystal electrode. Tartu, 2007, 180 p.

67. **Lauri Jalukse.** Measurement uncertainty estimation in amperometric dissolved oxygen concentration measurement. Tartu, 2007, 112 p.

68. **Aime Lust.** Charge state of dopants and ordered clusters formation in CaF_2:Mn and CaF_2:Eu luminophors. Tartu, 2007, 100 p.

69. **Iiris Kahn**. Quantitative Structure-Activity Relationships of environmentally relevant properties. Tartu, 2007, 98 p.

70. **Mari Reinik.** Nitrates, nitrites, N-nitrosamines and polycyclic aromatic hydrocarbons in food: analytical methods, occurrence and dietary intake. Tartu, 2007, 172 p.

71. **Heili Kasuk.** Thermodynamic parameters and adsorption kinetics of organic compounds forming the compact adsorption layer at Bi single crystal electrodes. Tartu, 2007, 212 p.

72. **Erki Enkvist.** Synthesis of adenosine-peptide conjugates for biological applications. Tartu, 2007, 114 p.

73. **Svetoslav Hristov Slavov**. Biomedical applications of the QSAR approach. Tartu, 2007, 146 p.

74. **Eneli Härk.** Electroreduction of complex cations on electrochemically polished Bi(*hkl*) single crystal electrodes. Tartu, 2008, 158 p.

75. **Priit Möller.** Electrochemical characteristics of some cathodes for medium temperature solid oxide fuel cells, synthesized by solid state reaction technique. Tartu, 2008, 90 p.

76. **Signe Viggor.** Impact of biochemical parameters of genetically different pseudomonads at the degradation of phenolic compounds. Tartu, 2008, 122 p.

77. **Ave Sarapuu.** Electrochemical reduction of oxygen on quinone-modified carbon electrodes and on thin films of platinum and gold. Tartu, 2008, 134 p.

78. **Agnes Kütt.** Studies of acid-base equilibria in non-aqueous media. Tartu, 2008, 198 p.

79. **Rouvim Kadis.** Evaluation of measurement uncertainty in analytical chemistry: related concepts and some points of misinterpretation. Tartu, 2008, 118 p.

80. **Valter Reedo.** Elaboration of IVB group metal oxide structures and their possible applications. Tartu, 2008, 98 p.

81. **Aleksei Kuznetsov.** Allosteric effects in reactions catalyzed by the cAMP-dependent protein kinase catalytic subunit. Tartu, 2009, 133 p.

82. **Aleksei Bredihhin.** Use of mono- and polyanions in the synthesis of multisubstituted hydrazine derivatives. Tartu, 2009, 105 p.

83. **Anu Ploom.** Quantitative structure-reactivity analysis in organosilicon chemistry. Tartu, 2009, 99 p.

84. **Argo Vonk.** Determination of adenosine A_{2A}- and dopamine D_1 receptor-specific modulation of adenylate cyclase activity in rat striatum. Tartu, 2009, 129 p.

85. **Indrek Kivi.** Synthesis and electrochemical characterization of porous cathode materials for intermediate temperature solid oxide fuel cells. Tartu, 2009, 177 p.

86. **Jaanus Eskusson.** Synthesis and characterisation of diamond-like carbon thin films prepared by pulsed laser deposition method. Tartu, 2009, 117 p.

87. **Marko Lätt.** Carbide derived microporous carbon and electrical double layer capacitors. Tartu, 2009, 107 p.

88. **Vladimir Stepanov.** Slow conformational changes in dopamine transporter interaction with its ligands. Tartu, 2009, 103 p.

89. **Aleksander Trummal.** Computational Study of Structural and Solvent Effects on Acidities of Some Brønsted Acids. Tartu, 2009, 103 p.

90. **Eerold Vellemäe.** Applications of mischmetal in organic synthesis. Tartu, 2009, 93 p.

91. **Sven Parkel.** Ligand binding to 5-HT_{1A} receptors and its regulation by Mg^{2+} and Mn^{2+}. Tartu, 2010, 99 p.

92. **Signe Vahur.** Expanding the possibilities of ATR-FT-IR spectroscopy in determination of inorganic pigments. Tartu, 2010, 184 p.

93. **Tavo Romann**. Preparation and surface modification of bismuth thin film, porous, and microelectrodes. Tartu, 2010, 155 p.

94. **Nadežda Aleksejeva.** Electrocatalytic reduction of oxygen on carbon nanotube-based nanocomposite materials. Tartu, 2010, 147 p.

95. **Marko Kullapere.** Electrochemical properties of glassy carbon, nickel and gold electrodes modified with aryl groups. Tartu, 2010, 233 p.

96. **Liis Siinor.** Adsorption kinetics of ions at Bi single crystal planes from aqueous electrolyte solutions and room-temperature ionic liquids. Tartu, 2010, 101 p.

97. **Angela Vaasa.** Development of fluorescence-based kinetic and binding assays for characterization of protein kinases and their inhibitors. Tartu 2010, 101 p.

98. **Indrek Tulp.** Multivariate analysis of chemical and biological properties. Tartu 2010, 105 p.

99. **Aare Selberg.** Evaluation of environmental quality in Northern Estonia by the analysis of leachate. Tartu 2010, 117 p.

100. **Darja Lavõgina.** Development of protein kinase inhibitors based on adenosine analogue-oligoarginine conjugates. Tartu 2010, 248 p.

101. **Laura Herm.** Biochemistry of dopamine D_2 receptors and its association with motivated behaviour. Tartu 2010, 156 p.

102. **Terje Raudsepp.** Influence of dopant anions on the electrochemical properties of polypyrrole films. Tartu 2010, 112 p.

103. **Margus Marandi.** Electroformation of Polypyrrole Films: *In-situ* AFM and STM Study. Tartu 2011, 116 p.

104. **Kairi Kivirand.** Diamine oxidase-based biosensors: construction and working principles. Tartu, 2011, 140 p.

105. **Anneli Kruve.** Matrix effects in liquid-chromatography electrospray mass-spectrometry. Tartu, 2011, 156 p.

106. **Gary Urb.** Assessment of environmental impact of oil shale fly ash from PF and CFB combustion. Tartu, 2011, 108 p.

107. **Nikita Oskolkov.** A novel strategy for peptide-mediated cellular delivery and induction of endosomal escape. Tartu, 2011, 106 p.

108. **Dana Martin.** The QSPR/QSAR approach for the prediction of properties of fullerene derivatives. Tartu, 2011, 98 p.

109. **Säde Viirlaid.** Novel glutathione analogues and their antioxidant activity. Tartu, 2011, 106 p.

110. **Ülis Sõukand.** Simultaneous adsorption of Cd^{2+}, Ni^{2+}, and Pb^{2+} on peat. Tartu, 2011, 124 p.

111. **Lauri Lipping.** The acidity of strong and superstrong Brønsted acids, an outreach for the "limits of growth": a quantum chemical study. Tartu, 2011, 124 p.

112. **Heisi Kurig.** Electrical double-layer capacitors based on ionic liquids as electrolytes. Tartu, 2011, 146 p.

113. **Marje Kasari.** Bisubstrate luminescent probes, optical sensors and affinity adsorbents for measurement of active protein kinases in biological samples. Tartu, 2012, 126 p.

114. **Kalev Takkis.** Virtual screening of chemical databases for bioactive molecules. Tartu, 2012, 122 p.

115. **Ksenija Kisseljova**. Synthesis of aza-β^3-amino acid containing peptides and kinetic study of their phosphorylation by protein kinase A. Tartu, 2012, 104 p.

116. **Riin Rebane.** Advanced method development strategy for derivatization LC/ESI/MS. Tartu, 2012, 184 p.

117. **Vladislav Ivaništšev.** Double layer structure and adsorption kinetics of ions at metal electrodes in room temperature ionic liquids. Tartu, 2012, 128 p.

118. **Irja Helm.** High accuracy gravimetric Winkler method for determination of dissolved oxygen. Tartu, 2012, 139 p.

119. **Karin Kipper.** Fluoroalcohols as Components of LC-ESI-MS Eluents: Usage and Applications. Tartu, 2012, 164 p.

120. **Arno Ratas.** Energy storage and transfer in dosimetric luminescent materials. Tartu, 2012, 163 p.

121. **Reet Reinart-Okugbeni**. Assay systems for characterisation of subtype-selective binding and functional activity of ligands on dopamine receptors. Tartu, 2012, 159 p.

122. **Lauri Sikk.** Computational study of the Sonogashira cross-coupling reaction. Tartu, 2012, 81 p.

123. **Karita Raudkivi.** Neurochemical studies on inter-individual differences in affect-related behaviour of the laboratory rat. Tartu, 2012, 161 p.

124. **Indrek Saar.** Design of GalR2 subtype specific ligands: their role in depression-like behavior and feeding regulation. Tartu, 2013, 126 p.

125. **Ann Laheäär.** Electrochemical characterization of alkali metal salt based non-aqueous electrolytes for supercapacitors. Tartu, 2013, 127 p.

126. **Kerli Tõnurist.** Influence of electrospun separator materials properties on electrochemical performance of electrical double-layer capacitors. Tartu, 2013, 147 p.

127. **Kaija Põhako-Esko.** Novel organic and inorganic ionogels: preparation and characterization. Tartu, 2013, 124 p.

128. **Ivar Kruusenberg.** Electroreduction of oxygen on carbon nanomaterial-based catalysts. Tartu, 2013, 191 p.

129. **Sander Piiskop.** Kinetic effects of ultrasound in aqueous acetonitrile solutions. Tartu, 2013, 95 p.

130. **Ilona Faustova**. Regulatory role of L-type pyruvate kinase N-terminal domain. Tartu, 2013, 109 p.

131. **Kadi Tamm.** Synthesis and characterization of the micro-mesoporous anode materials and testing of the medium temperature solid oxide fuel cell single cells. Tartu, 2013, 138 p.

132. **Iva Bozhidarova Stoyanova-Slavova.** Validation of QSAR/QSPR for regulatory purposes. Tartu, 2013, 109 p.

133. **Vitali Grozovski**. Adsorption of organic molecules at single crystal electrodes studied by *in situ* STM method. Tartu, 2014, 146 p.

134. **Santa Veikšina**. Development of assay systems for characterisation of ligand binding properties to melanocortin 4 receptors. Tartu, 2014, 151 p.

135. **Jüri Liiv.** PVDF (polyvinylidene difluoride) as material for active element of twisting-ball displays. Tartu, 2014, 111 p.

136. **Kersti Vaarmets.** Electrochemical and physical characterization of pristine and activated molybdenum carbide-derived carbon electrodes for the oxygen electroreduction reaction. Tartu, 2014, 131 p.

137. **Lauri Tõntson**. Regulation of G-protein subtypes by receptors, guanine nucleotides and Mn^{2+}. Tartu, 2014, 105 p.

138. **Aiko Adamson.** Properties of amine-boranes and phosphorus analogues in the gas phase. Tartu, 2014, 78 p.

139. **Elo Kibena**. Electrochemical grafting of glassy carbon, gold, highly oriented pyrolytic graphite and chemical vapour deposition-grown graphene electrodes by diazonium reduction method. Tartu, 2014, 184 p.

140. **Teemu Näykki.** Novel Tools for Water Quality Monitoring – From Field to Laboratory. Tartu, 2014, 202 p.

141. **Karl Kaupmees.** Acidity and basicity in non-aqueous media: importance of solvent properties and purity. Tartu, 2014, 128 p.

142. **Oleg Lebedev**. Hydrazine polyanions: different strategies in the synthesis of heterocycles. Tartu, 2015, 118 p.

143. **Geven Piir.** Environmental risk assessment of chemicals using QSAR methods. Tartu, 2015, 123 p.

144. **Olga Mazina.** Development and application of the biosensor assay for measurements of cyclic adenosine monophosphate in studies of G protein-coupled receptor signalinga. Tartu, 2015, 116 p.

145. **Sandip Ashokrao Kadam.** Anion receptors: synthesis and accurate binding measurements. Tartu, 2015, 116 p.

146. **Indrek Tallo.** Synthesis and characterization of new micro-mesoporous carbide derived carbon materials for high energy and power density electrical double layer capacitors. Tartu, 2015, 148 p.

147. **Heiki Erikson.** Electrochemical reduction of oxygen on nanostructured palladium and gold catalysts. Tartu, 2015, 204 p.

148. **Erik Anderson.** *In situ* Scanning Tunnelling Microscopy studies of the interfacial structure between Bi(111) electrode and a room temperature ionic liquid. Tartu, 2015, 118 p.

149. **Girinath G. Pillai.** Computational Modelling of Diverse Chemical, Bio-chemical and Biomedical Properties. Tartu, 2015, 140 p.

150. **Piret Pikma.** Interfacial structure and adsorption of organic compounds at Cd(0001) and Sb(111) electrodes from ionic liquid and aqueous electrolytes: an *in situ* STM study. Tartu, 2015, 126 p.

151. **Ganesh babu Manoharan.** Combining chemical and genetic approaches for photoluminescence assays of protein kinases. Tartu, 2016, 126 p.

152. **Carolin Siimenson**. Electrochemical characterization of halide ion adsorption from liquid mixtures at Bi(111) and pyrolytic graphite electrode surface. Tartu, 2016, 110 p.

153. **Asko Laaniste.** Comparison and optimisation of novel mass spectrometry ionisation sources. Tartu, 2016, 156 p.

154. **Hanno Evard.** Estimating limit of detection for mass spectrometric analysis methods. Tartu, 2016, 224 p.

155. **Kadri Ligi.** Characterization and application of protein kinase-responsive organic probes with triplet-singlet energy transfer. Tartu, 2016, 122 p.

156. **Margarita Kagan.** Biosensing penicillins' residues in milk flows. Tartu, 2016, 130 p.

157. **Marie Kriisa.** Development of protein kinase-responsive photo-luminescent probes and cellular regulators of protein phosphorylation. Tartu, 2016, 106 p.

158. **Mihkel Vestli.** Ultrasonic spray pyrolysis deposited electrolyte layers for intermediate temperature solid oxide fuel cells. Tartu, 2016, 156 p.

159. **Silver Sepp**. Influence of porosity of the carbide-derived carbon on the properties of the composite electrocatalysts and characteristics of polymer electrolyte fuel cells. Tartu, 2016, 137p.

160. **Kristjan Haav**. Quantitative relative equilibrium constant measurements in supramolecular chemistry. Tartu, 2017, 158 p.

161. **Anu Teearu**. Development of MALDI-FT-ICR-MS methodology for the analysis of resinous materials. Tartu, 2017, 205 p.
162. **Taavi Ivan**. Bifunctional inhibitors and photoluminescent probes for studies on protein complexes. Tartu, 2017, 140 p.
163. **Maarja-Liisa Oldekop**. Characterization of amino acid derivatization reagents for LC-MS analysis. Tartu, 2017, 147 p.
164. **Kristel Jukk**. Electrochemical reduction of oxygen on platinum- and palladium-based nanocatalysts. Tartu, 2017, 250 p.
165. **Siim Kukk**. Kinetic aspects of interaction between dopamine transporter and *N*-substituted nortropane derivatives. Tartu, 2017, 107 p.
166. **Birgit Viira**. Design and modelling in early drug development in targeting HIV-1 reverse transcriptase and Malaria. Tartu, 2017, 172 p.
167. **Rait Kivi**. Allostery in cAMP dependent protein kinase catalytic subunit. Tartu, 2017, 115 p.
168. **Agnes Heering**. Experimental realization and applications of the unified acidity scale. Tartu, 2017, 123 p.
169. **Delia Juronen**. Biosensing system for the rapid multiplex detection of mastitis-causing pathogens in milk. Tartu, 2018, 85 p.
170. **Hedi Rahnel.** ARC-inhibitors: from reliable biochemical assays to regulators of physiology of cells. Tartu, 2018, 176 p.